Accepted Manuscript

Geological Society, London, Special Publications

Petrology of the explosive deposits from the April 2021 eruption of La Soufrière volcano, St Vincent: a time-series analysis of microlites

H. M. Frey, M. R. Manon, J. Barclay, B. V. Davies, S. A. Walters, P. D. Cole, T. E. Christopher & E. P. Joseph

DOI: https://doi.org/10.1144/SP539-2022-291

To access the most recent version of this article, please click the DOI URL in the line above. When citing this article please include the above DOI.

Received 21 September 2022
Revised 13 February 2023
Accepted 14 February 2023

Supplementary material at https://doi.org/10.6084/m9.figshare.c.6534864

Petrology of the explosive deposits from the April 2021 eruption of La Soufrière volcano, St Vincent: a time-series analysis of microlites

H. M. Frey[1*], M. R. Manon[1], J. Barclay[2], B. V. Davies[2], S. A. Walters[1], P. D. Cole[3], T. E. Christopher[4], and E. P. Joseph[5]

[1]Geoscience Department, Union College, NY 12308 Schenectady, United States

[2]School of Environmental Sciences, University of East Anglia, NR4 7TJ Norwich, United Kingdom

[3]School of Geography, Earth and Environmental Sciences, University of Plymouth, PL4 8AA Plymouth, United Kingdom

[4]Montserrat Volcano Observatory, Montserrat, Flemmings, Montserrat, West Indies

[5]University of West Indies Seismic Research Centre, St. Augustine, Trinidad & Tobago, West Indies

ORCID ID: HF, 0000-0002-3981-9043

* Corresponding author (freyh@union.edu)

Abstract

After more than three months of lava dome extrusion, La Soufrière (St. Vincent) transitioned to a series of explosive eruptions in April 2021. Here we present a time-series petrologic analysis of the phenocryst and microlite populations during the first ~48 hours of explosivity to constrain ascent conditions and processes that drove changes in behavior. Primary eruptive products were crystal-rich (45-50 vol%) basaltic andesites with similar phenocryst phase assemblages and compositions. The change in eruptive style is consistent with overpresurization as a consequence of second boiling from anhydrous microlite crystallization. The microlites display variation between the explosive phases, with two populations: 1) "inherited" - normally zoned high-An plagioclase (>An_{70}) + olivine (Fo_{62-79}) + clinopyroxene + titanomagnetite, inferred to have crystallized at depths >15 km and high water pressures; 2) "juvenile" - unzoned plagioclase (An_{45-65}) + clinopyroxene + orthopyroxene + intermediate pyroxene (Wo_{12-38}) + titanomagnetite, inferred to have crystallized upon ascent due to decompression and degassing. Scoria from the first explosions featured extensive groundmass crystallization and a significant "inherited" microlite population. Later explosions had a more abundant "juvenile" microlite population and lower crystallinity, consistent with more rapid ascent from depth, initiated by decompression following initial blasts and destruction of the lava dome.

Keywords

Microlites, Eruption triggers, Ascent, Second boiling, St. Vincent, Lesser Antilles Arc

Supplementary material: Tables of sample locations, all electron microprobe analyses, and CSD measurements are available at https://doi.org/10.6084/m9.figshare.c.6534864.

Introduction

Like many arc stratovolcanoes, La Soufrière volcano, located on the Eastern Caribbean island of St. Vincent, is characterized by both effusive and explosive behavior, presenting a considerable challenge in anticipating the nature of activity prior to its onset. On April 9th, 2021, after more than 3 months of effusive eruptions and lava dome growth, La Soufrière erupted explosively, with a series of >30 Vulcanian and sub-Plinian eruptions, which ceased on April 22, 2021. Less than 24 hours before the explosive eruptions began, the local seismic network recorded banded tremors, indicative of an imminent explosive phase, after swarms of volcano-tectonic (VT) earthquakes were recorded in late March and early April, 2021 (Joseph *et al.* 2022). Following the eruptions, a stratigraphically constrained sampling of several units within the tephra-fall deposits (Cole et al., this volume) has allowed us to do a comprehensive petrologic time-series study through the first 48 hours of the deposits from the explosive eruption(s), documenting the mineral assemblages, compositions, and textures as the eruption(s) progressed.

The eruptive products of stratovolcanoes at volcanic arcs often feature a complex crystal cargo, which can be interrogated to ascertain the nature of plumbing systems via magma storage conditions at transient or long-term equilibrium (e.g., temperature, pressure, volatile content), and dynamic changes that occur in the conduit as the magma ascends to the surface. Phenocryst core compositions can address the former, whereas microlites and/or crystal rims can offer insights into the latter. Mineral assemblage compositions and textures also allow for the exploration of the possible mechanisms that initiate and/or trigger eruptions and change in eruptive style (e.g., effusive to explosive). Various internal processes such as magma injection into a pre-existing reservoir (e.g. Sparks *et al.* 1977; Eichelberger and Izbekov 2000; Humphreys *et al.* 2006; Ruprecht and Wörner 2007; Kent *et al.* 2010; Druitt *et al.* 2012), magma buoyancy (e.g. Caricchi *et al.* 2014; Malfait *et al.* 2014), volatile exsolution of magma (e.g. Kent *et al.* 2007; Stock *et al.* 2016; Caricchi *et al.* 2018; Cassidy *et al.* 2018) and fluid fluxing from depth (e.g. Petrelli *et al.* 2018; Utami *et al.* 2021, 2022) have been invoked as possible eruption triggers. In contrast, eruptive style may be controlled by magma ascent and decompression rate (e.g. Gonnermann and Manga 2007) or be a function of pre-eruptive crystallinity, dissolved water content, and the water saturation state/temperature of the melt (e.g. Popa *et al.* 2021).

During magma ascent, groundmass crystallization of microlites often occurs as a result of decompression-induced degassing and thus serves as a record of processes during magma ascent (e.g. Cashman 1992; Hammer *et al.* 1999). Microlite or crystal size distribution (CSD) analyses and slopes can be used to infer changing crystallization conditions at late stages before eruption (e.g.

Cashman and Marsh 1988; Castro *et al.* 2003; Toramaru *et al.* 2008; Mangler *et al.* 2022). The transition between effusive and eruptive styles can be recorded by changes in microlite texture and composition (e.g. Cashman and McConnell 2005; Castro and Gardner 2008; Martel 2012; Preece *et al.* 2013; Mujin and Nakamura 2014; Murch and Cole 2019). In addition to giving insights into decompression rates and eruptive styles, microlites can record crystallization as a result of cooling (Lormand *et al.* 2020) or reflect magma mixing of crystals formed at greater depths or in mafic melts (Martel *et al.* 2006; Humphreys *et al.* 2009; Lormand *et al.* 2021).

As recently noted by Re *et al.* (2021), detailed petrologic studies of eruptive products are an underutilized tool in volcanic risk assessment and hazard management and may provide key insights into magmatic process and initiation of eruptions, which can in turn be used to anticipate likely monitoring signals that might herald these processes during an eruption. Recent syn-eruptive petrologic work at Mt. Etna (Corsaro and Miraglia 2022) and La Palma (Pankhurst *et al.* 2022) has demonstrated the utility of documenting changes in the melt/magma during ongoing eruptions. In this study, we offer a detailed petrologic analysis of microlite abundances, textures and compositions of basaltic-andesite scoria from proximal and distal locations, erupted during successive Vulcanian explosions over a 48-hour period, beginning April 9th, 2021, following a >three-month period of lava dome extrusion at La Soufrière volcano. A critical feature of our dataset is its integration with the time-constrained stratigraphy of the explosive events (Cole et al., this volume), and the comparison with geophysical datasets collected during the volcanic crisis by the University of the West Indies Seismic Research Center (UWI-SRC) (Joseph *et al.* 2022, Camejo-Harry *et al.* this volume, Sparks *et al.* this volume). Complementary petrologic studies on the pre-eruptive storage conditions and dome materials (Weber *et al.* this volume), experimental constraints on crystallization (Morrison Evans *et al.* this volume), the rheology of effusive and explosive magmas (Sparks *et al.* this volume), and vesicle/bubble size distribution (Christopher *et al.* this volume) provide further important context for this study. We demonstrate that the microlite population varied considerably through the course of this eruptive sequence offering a unique insight into the changing subsurface conditions of this explosive sequence.

Recent volcanic history and experimental petrology of La Soufrière St. Vincent

La Soufrière stratovolcano, located in northern St. Vincent (Fig. 1), is amongst the most active volcanic systems in the Eastern Caribbean, with 6 documented eruptions in the historic record, occurring in 1979, 1971-72, 1902-03, 1812, 1784 and 1718 (Cole *et al.* 2019). These eruptions represent either dominantly effusive or explosive events, although some transitioned between styles during the course of an eruption (Robertson et al., this volume). However, they are compositionally

restricted to basaltic andesites and dominated by scoria-bearing pyroclastic density currents, with subordinate fallout deposits (Robertson 1995; Cole *et al.* 2019; Fedele *et al.* 2021).

Several experimental studies (e.g. Pichavant *et al.* 2002; Pichavant and Macdonald 2007; Melekhova *et al.* 2015) have illuminated the generation, storage and evolution of relevant basaltic melts, as well providing specific detailed examinations of cumulate/xenoliths from St. Vincent (Arculus and Wills 1980; Heath *et al.* 1998; Tollan *et al.* 2012; Melekhova *et al.* 2015; Fedele *et al.* 2021). Fedele *et al.* (2021) suggested that the plumbing system beneath St. Vincent is a vertically extensive crystal mush comprised of multiple crustal differentiation/storage zones, with a shallow zone at 3.5-7 km and a deeper source at >13 km. These depths are comparable to what has been described for the nearby islands of Montserrat (5-16 km; Edmonds *et al.* 2016), Bequia (up to 34 km; Camejo-Harry *et al.* 2018) and Grenada (7-17 km; Stamper *et al.* 2014).

2021 Eruption summary: geophysical and stratigraphic context of the studied samples

In November 2020, the La Soufrière system began to generate very low-level seismicity. On Dec. 27, 2020, a new lava dome emerged on the SW perimeter of the 1979 lava dome. Over the ensuing three months, extrusion of viscous lava continued and formed an elongated coulee (Stinton *et al.* this volume). Prior to the onset of the explosive sequence a swarm of VT (volcano-tectonic) earthquakes occurred. These were located at relatively shallow depths (~5 km) and interpreted as a consequence of breaking rock and fluids moving through cracks. A second VT swarm was detected on April 5th, but at depths >10 km (Joseph *et al.* 2022). Following these short-lived VT swarms, on April 8th banded tremor, or bursts of low frequency earthquakes, were detected with a continuous seismic signal. A sequence of explosive eruptions began ~8:41 am AST/12:41 UTC on April 9th, generating eruption plumes in excess of 10 km. The first explosion seems to be located closer to the surface in an attempt to remove the remaining material of the overlying dome and cap. Subsequent explosions show a deepening sequence (2.5 - 4.0 km) (Contreras-Arratia, pers comm.). This also coincided with a rapid deflation detected by InSAR around the summit of the volcano (Camejo-Harry et al., this volume).

Monitoring of hydrothermal waters on the western flanks of the volcano in February, March, and April, 2021 showed increases in water temperature, but no corresponding changes in composition (Christopher *et al*. this volume). Collectively, these geochemical signals and apparent lack of degassing suggest minimal SO_2 degassing and potential scrubbing by the shallow hydrothermal system during the effusive phase of the eruption. Alternatively, gas escape could have been trapped at the base of the conduit due to the impermeable nature of the lava dome an

volcanic edifice (Joseph *et al.*, 2022). MultiGAS monitoring during the effusive phase was also dominated by a hydrothermal signature with little detection of SO_2 until late March. Commensurate with the VT earthquakes on March 23rd, an increase in the amount of CO_2 gas was measured and the day prior to explosive activity, a weak SO_2 plume (80 tons/day) was detected (Joseph *et al.* 2022).

Using a combination of field-based stratigraphy and eye-witness accounts, Cole *et al.* (this volume) have recognized 7 different stratigraphic units associated with different phases of explosive activity between the 9th and 22nd of April. The first unit (U1) is associated with the first ~24 hours, when explosions were largely pulsatory in nature, following the initial explosion. The descending sequence of seismicity largely occurred in the hiatus between this distinctive U1 explosion and this pulsatory sequence. A series of explosive eruptions of varying size and duration continued until April 22nd, with the recognition of >30 events. These explosions deposited significant amounts of ash throughout St. Vincent and the Grenadines, as well as the neighboring islands of Barbados and St. Lucia. In addition to tephra-fall, laterally extensive pyroclastic density currents commenced at the onset of U3 explosions later on the afternoon of April 10th (Cole *et al*. this volume).

The pre-eruptive conditions of the 2020-21 La Soufrière magmatic system are explored by Weber *et al.* (this volume), based on petrologic analysis of samples from the 2021 lava dome collected in January 2021 and scoria from explosions associated with U5. Weber *et al.* (this volume) found a comparable phase assemblage and mineral compositions between the effusive lava dome and explosive scoria samples. Using K_D (distribution coefficients) between minerals and between minerals and the groundmass glass, they demonstrate minerals were largely not in chemical equilibrium with each other or the host liquid or carrier melt, which was estimated to be andesitic (60 to 63 wt. % SiO_2). Thermobarometery suggests that crystallization of (some) phenocrysts likely occurred between 8 and 13 km depth at temperatures of 997^{+18}_{-35} °C. Weber *et al.* (this volume) concluded that the change in eruptive style at La Soufrière was not controlled by plumbing system architecture or magma composition, but that the transition may reflect outgassing efficiency during magma ascent. Further, there was no petrologic evidence to support mafic injection/rejuvenation, as a mechanism.

To explore the drivers of the explosive eruptive phase, we focused our petrologic investigation on the compositions, abundances, and sizes of microlites in vesicular scoria from the earliest explosive deposits that occurred April 9th-10th, 2021 in four different units (Cole *et al.* this volume). An additional study, Christopher et al. (this volume), documents the changes in vesicularity in these same units and the volcanic outgassing over the course of the eruption.

Materials and Methods

Eruptive deposits and sampling

All samples analysed in this study were collected during three sampling campaigns and are from fall deposits of Vulcanian and/or sub-Plinian explosions that occurred within the first 48 hours of the explosive activity. The samples stratigraphically belong to units U1, U2, U3, and U5 (Fig. 2) and drew from the vesicular scoria population in these units, assumed to represent contemporary quenched magma (Cole et al., this volume). U4 samples were not analysed, as the unit is a fine-grained ash that lacks significant scoria. We briefly summarise the inferred timings of samples from Cole et al. (this volume) here. U1 samples are associated with the initial 'pulsatory' explosions from 12:35 UTC on 9th April to 09:30 on 10th April. U2 samples are from ash-rich deposits and semi-continuous eruptions that occurred from the later morning into the afternoon on the 10th April. U3 marked the onset of pyroclastic density currents during the evening and overnight on the 10th April and generated coarse vesicular lapilli from its explosions, as well as the first pyroclastic density currents. U5 is inferred to have commenced early on 11th April and generated the coarsest vesicular scoria clasts. Scoria samples from U5 were collected along the banks of the Rabacca River, east of the volcano summit north of Georgetown, on April 11th, 2021 and measure up to 4 cm in diameter. Smaller scoria clasts from (4-8 mm in diameter) from U1 and U2 were collected in late April 2021. To access larger clasts from these important horizons (U1 and U2), vesicular scoria samples representing U1, U2, U3, and U5 were collected from a single locality on the south-eastern flanks of the volcano in the region near Jacobs Well (~0.5-1 km from the crater rim) in January 2022 (Fig. 2). These were several cm in diameter. This final sampling campaign ensured that there was not a location or sample size bias that influenced the data obtained from our initial characterization of the units, when sample availability and size was more limited. Description of the sampled materials and locations are listed in supplementary Table 1. Additional petrological analyses of scoria from U5 and lava from the 2021 lava dome were obtained by Weber *et al.* (this volume).

Analytical methods

Scanning electron microscopy (SEM) qualitative imaging

As an initial investigative tool, back-scattered electron images (BSE) of 22 clasts (U1, U2, U3, U5) were collected on a Zeiss EVO-50 scanning electron microscope (SEM) at Union College, using a 15 keV accelerating voltage with a current of approximately 1 nA. This allowed us to determine phase assemblages, abundances, textures, and compositional zoning features across the various units and establish the homogeneity (or lack thereof) in multiple scoria clasts within the same unit. Preliminary

energy dispersive X-ray (EDS) analyses were acquired using the Bruker XFlash 6130 detector on cores and rims of crystals to establish broad patterns amongst the phenocrysts and microlites. From these preliminary results, select thin-sections were more rigorously analyzed by electron microprobe analysis.

Proportions of the various mafic microlite phases (olivine, clinopyroxene, orthopyroxene) were determined on the SEM. For each thin-section, 15-20 high contrast BSE images were acquired from 3-5 regions in each scoria clast. Qualitative chemical compositions from all mafic microlites large enough to produce reliable EDS spectra (> 5 µm in width) were measured to assess relative proportions of the mafic phases. Because clinopyroxene and orthopyroxene display identical BSE grayscale brightness for these compositions, EDS was required to differentiate between them and an automated image analysis routine could not be employed. Olivine microlites (and phenocrysts) are brighter in BSE than pyroxenes, and often featured a brighter, thin (<5 um), iron enriched rim, in sharp contact with a more Mg-rich core. The BSE images were also used to determine the relative proportion of zoned versus un-zoned plagioclase microlites. Optimizing for this contrast obscured any variability in magnetite brightness. However, imaging at lower brightness/contrast, combined with probe analyses revealed remarkable homogeneity and lack of exsolution in magnetite microlites from the explosive activity.

Electron microprobe analysis (EMPA)

Based on initial reconnaissance imaging and analysis, 14 thin-sections were selected for further investigation. Major and select trace element analyses of phenocrysts, microlites, and groundmass glass were determined by electron microprobe using the Cameca SXFive-TACTIS in the Electron Microprobe lab of the Geosciences department at the University of Massachusetts at Amherst. The electron beam was operated at 15 kV and 20 nA. Peak times were typically 20-30 seconds per element, with sodium and potassium counted first in all glass and feldspar analyses. To avoid sample heating in the beam sensitive glass and feldspars, we used an open beam, at widths of 5 and 3 µm, respectively. Due to their small size, plagioclase microlites were measured using a focused beam. Perhaps due to their calcic nature (> 40 mol % An), phenocryst compositions measured using the focused beam show no systematic difference to those from the 3 µm beam, so we did not employ a Na sub-counting routine. Background spectra were acquired once per analysis setup (about every 10-30 points). Standardization was performed using the in-house natural standards at UMass, typically using z-matched silicates. Calibration was checked by analytical total, as well as against secondary standards, such as labradorite PG-721 for feldspars. Phi-Rho-Z matrix corrections were performed using the Cameca SX software. Analytical uncertainties are derived from counting

statistics and at the 3-sigma level for olivines are 0.24-0.5 wt % for major elements (Si, Fe, Mg) and 0.01-0.04 wt % for minor and trace elements, which results in an average of 2 mol% error in derived Fo. For pyroxenes, major element uncertainties range from 0.1 to 0.4 wt% (Si, Fe, Mg, Ca) and are 0.01-0.05 wt% for minor elements. Ferric iron in pyroxenes is estimated by balancing a charge of -12 for formulas normalized to 4 cations. This results in a mean value of 0.065 Fe3+ p.f.u. for cpx and 0.015 for opx. Uncertainty on major elements in feldspars range from 0.1-0.3 wt%, and are an order of magnitude lower for minor and trace components. This yields an uncertainty of ~1 mol% An derived from these analyses. For titanomagnetites, analytical uncertainty is dominated by the measurement of total iron, which is on average 1 wt%. Other major elements have analytical uncertainties of 0.03-0.08 wt% and minor/trace elements are all around 0.01 wt %. Molar proportions are normalized to 3 cations and the proportion of ferric vs ferrous iron is calculated to balance the charge of four oxygens, assuming iron is the only multivalent element. The result is a relative uncertainty in calculated Usp and Hem parameters of 2.2 %. For groundmass glass, uncertainty ranges from 0.1 to 0.3, and 0.02-0.09 for major and minor/trace elements, respectively.

Representative analyses of each phenocryst/microlite phase are presented in Table 1, with additional analyses in the supplementary material. The compositional classification of the mineral phases is based on major elemental components. For plagioclase, anorthite (An) is the molar percentage of An/(An+Ab+Or). In olivine, the forsterite (Fo) component is the molar percentage of Fo/(Fo+Fa). Pyroxene is classified with respect to Mg# (Mg/(Mg +Fe)) or the enstatite (En) component (En/(En+Fs+Wo)), which considers the abundance of calcium. Ulvospinel is calculated as $Fe^{2+}/(Fe^{2+}+Fe^{3+}+Ti)$. Phenocrysts are defined as being >100 μm in length. Smaller crystalline phases are defined as microphenocrysts (30-100 μm in length) and microlites (<30 μm in length). There is also a significant population of smaller crystals, which cannot be analyzed by EMPA due to their small size (<5 μm), but are a key component in the crystal size distribution (CSD) analysis. Additional BSE imaging at higher resolution was used for the CSD, as described below.

Groundmass analyses of the dome and U3 and U5 scoria were done by Weber *et al.* (this volume) using a 20 μm defocused beam over both glass and microlites. In this study, we attempted to analyze the residual melt or glass composition that was devoid of microlites. Small pockets (~5 μm) of melt between microlites were targeted for analysis and a filtering protocol was employed to eliminate contamination by crystalline phases adjacent to or beneath the glass.

To start, we impose a loose total filter (>94 and <101 wt). To eliminate unseen contamination by microlite phases, analyses with high Al_2O_3 (>20 wt%, feldspars), and those with high values of Mn/K (mafic phases) were discarded. Data is available in supplementary tables.

Wavelength dispersive spectroscopy (WDS) mapping

Full thin-section WDS elemental mapping was done on 9 thin-sections (U1-U5) at UMass Amherst with the Cameca SX100. Four WDS spectrometers were focused on the k-alpha line of a different element (Mg, Ca, Fe, Al), and other elements (K, Na, Si, Ti) were simultaneously collected using the EDS. The section was gridded, with point analyses taken every 30 µm, allowing us to capture phenocryst phases and capture any variance between samples. The resolution of the WDS maps was not sufficient to characterize the microlite populations; this is described below.

Crystal size distribution analysis (CSD)

Back-scatter electron (BSE) micrograph images of the same samples used for the petrographic and geochemical analysis were obtained using Scanning Electron Microscopy (SEM) imaging at the University of East Anglia (Zeiss Gemini 300 field emission SEM with Oxford Instruments Ultim Max 170 EDS). Imaging and analysis were conducted at 10 kV with a working distance of 8.5 mm. For scoria, images were collected at 460x magnification, with an image resolution of ~ 16 px/µm (Fig. S1). For dome rocks, images were collected between 444x and 1.07kx, with an image resolution of 4 - 9.4 px/µm. Proportions of vesicles, clinopyroxene, and Fe-Ti oxides were acquired through thresholding of BSE images in Image-J software. Plagioclase microlites were manually identified using image analysis software and then the key characteristics of the crystal outlines quantified using Image-J software. 2D-3D conversion and shape analysis was performed using SHAPECALC (Mangler *et al.* 2022) and plotted in Zingg diagrams. Crystal shapes are classified based on ratios of 3D short (*S*) to intermediate (*I*) to long (*L*) axes, plotted as 3D *I*/*L* against 3D *S*/*I.* CSD curves were plotted using *CSD Corrections* v1.6 (Higgins 2000). At least 600 crystals were measured from each analyzed sample to produce a stable CSD curve. Use of a single shape factor in production of a CSD curve may impact the overall shape of the CSD, as crystal shape changes with size. However, sub-dividing the CSD into manually defined crystal size bins which are then analysed using individual shape factors in CSDCorrections could introduce artifacts that cannot be easily constrained at this time. Thus, we used only one shape factor for each analyzed sample (Mangler *et al*., 2022).

Phase proportions, mean area and calculated aspect ratios for crystals < 100 um (long axis) are summarized in Table 2. Note that for % crystals, olivine and pyroxene are grouped together as "mafics" due to their brightness similarity in BSE images that were optimized for plagioclase CSD analysis. A more detailed breakdown of the crystalline mafic component is provided in Table 3, based on high-contrast BSE images and EDS spectral analysis. However, the relative proportion of

mafic crystals in Table 3 are restricted to crystals >5 µm, which contrasts with the crystals considered for Table 2.

Results

Like many of the previous eruptions on St. Vincent (e.g. Graham and Thirlwall 1981; Heath *et al.* 1998; Fedele *et al.* 2021), the 2021 explosive eruptions of La Soufrière are characterized by a complex crystal cargo that includes xenoliths/xenocrysts, glomerocrysts, phenocrysts, and microlites. Texturally, the scoria samples are crystal-rich (~40-45 vol%) and porphyritic (Fig. 3), with little variation in phenocrysts observed between samples. Crystal clusters are ubiquitous in the scoria samples and were classified as glomerocrysts (euhedral/subhedral crystals that are touching along margins, Fig. 4e) or xenocrysts (granular to intergranular textures and intergrowths). Rare rock fragments (Fig. 4f) with breakdown textures (e.g. hydrothermal alteration from fluids) were also noted and are similar to textures observed in the summit lava domes (Joseph *et al.* 2022; Weber *et al*. this volume). The phase assemblage includes abundant plagioclase, plus clinopyroxene, orthopyroxene, olivine, and titanomagnetite in a vesicular, microlite-rich groundmass (Fig. 4). Thus, the compositional range of the various phenocryst mineral phases in all of the explosive units (U1-U5), and the 2020-21 lava dome (Weber *et al.* this volume) are broadly similar. Euhedral crystal morphology, faceted crystal faces, and lack of reverse zoning, coronas, overgrowths, resorption, breakdown or sieve textures suggest textural equilibrium. Despite this, a significant proportion of phenocrysts and glomerocrysts are likely *not* in chemical equilibrium (Weber *et al*., this volume, see below). The xenocrysts and rock fragments are further evidence of entrainment of phenocrystic material by the carrier melt of the 2021 eruption, but are beyond the scope of this paper and not discussed further. The most distinctive feature of the scoria between explosive units is thus the differing relative abundance, composition, and size of the microlites (this study), as well as the vesicle size distribution (Christopher *et al.* this volume), as the eruption progressed.

Phenocrysts

Although we analyzed additional units, we found our phenocryst populations comparable to that of Weber et al. (this volume). Therefore, we only introduce these briefly below to provide a contrast to microlite analyses.

Plagioclase phenocrysts within all the explosive units vary widely in size, from 100 – 1500 µm in length (with a few even larger) and span the same, broad compositional range in anorthite, from An_{48} to An_{98}, that Weber *et al.* (this volume) reported for the 2021 lava dome and a different sub-set of U5 scoria clasts (Fig. 5). The majority of plagioclase phenocrysts are unzoned, with a subordinate

proportion that feature strong normal zoning (Fig. 4b), and a few with weak, patchy or oscillatory zoning. With respect to diagnostic minor elements such as FeOt and TiO_2, there does not appear to be a discernible difference between most phenocryst cores (>An_{65}) and rims (<An_{65}) (Fig. 6a), with the exception of the most calcic (>An_{80}) cores, which have lower FeOt concentrations.

Olivine phenocrysts within all explosive units have a similar euhedral morphology and composition, with cores ranging from Fo_{67} to Fo_{80}. Many of the phenocrysts and the majority of microphenocrysts/microlites feature thin, <5 µm distinctive rims that appear very bright in BSE, likely indicating a higher Fe concentration than the host crystal. The narrow width of these rims precludes microprobe analysis, but EDS elemental maps, and mixed spectra analysis (rims + matrix) indicate significant iron enrichment. Trace element abundances (e.g. Ni, Cr, Mn, and Ca) are similar across the units, as exemplified by CaO concentrations (Fig. 6b).

Pyroxene phenocrysts within all three explosive units have sharp, euhedral edges, are unzoned, and have a restricted range in composition (Mg#69-87 for cpx and Mg#63-72 for opx) that is comparable throughout the successive explosions (Fig. 6c) and that is virtually identical to the median pyroxene composition reported by Weber *et al*. (this volume) for the U5 scoria and 2021 lava dome.

Fe-Ti oxides form a single population classified as titanomagnetite, with little compositional variation, recording ulvöspinel fractions of 0.39 to 0.48, with the majority of analyses clustered at 0.44-0.46 and TiO_2 ~13-14 wr% (Fig. 6d). Unlike the titanomagnetite in the lava dome (Weber *et al.* this volume), the titanomagnetite in the scoria is homogeneous, with no evidence for exsolution.

Groundmass glass

The glass analyses reflect the melt composition and effects of crystallization and vary by up to 11% SiO_2 in a single scoria clast (Fig.7). Glass analyses from U5 demonstrate the least compositional variance and yield the highest totals (99.6 ± 0.88 on average), compared with 97.3±1.9, 97.5±2.1, and 97.1±1.3 for U1, U2, and U3 respectively. This may suggest that the later (≥U5) explosions were quenched when relatively depleted in volatiles. When analyses of silica are normalized to an anhydrous melt (100%), the average values are dacitic (64.9 ± 2.1). U1 clasts have an average SiO_2 content of 63.5 wt% (+/- 2.3 wt% at 1 SD), U2 has an average SiO_2 content of 64.8 wt% (+/- 2.0 wt% at 1 SD), U3 has an average SiO_2 content of 65.6 wt% (+/- 1.6 wt% at 1 SD) and U5 has an average SiO_2 content of 65.9 wt% (+/- 1.8 wt% at 1 SD). Given the large range and standard deviations of the analyses within each unit (Fig. 7) and indeed within individual thin sections, the analyzed point melt compositions reflect the effects of local crystallization of microlites. But, the

apparently lower average value of SiO_2 for the more microlite-rich U1 clasts is then counterintuitive, and so the compositions of the groundmass glass *may* be slightly less evolved in U1. However, the large variance and analytical error preclude a definitive assessment of possible changes in the melt as the eruption progressed. Weber *et al.* (this volume) employed several different approaches to assess the groundmass (glass + microlites) composition of U5 scoria and this is shown for comparison (Fig. 7).

Microlites in scoria

The groundmass of the 2021 La Soufrière explosive deposits is characterized by being very microlite-rich (>25% vol, based on a vesicle-free normalization), with the same phase assemblage (plag + cpx + opx + ol + ttm) as the phenocryst population (Fig. 8). However, unlike the phenocryst populations, there appear to be systematic differences in sizes, shapes, and relative abundances and compositions of the microlites across the eruptive sequences. Scoria clasts within the same unit yield similar relative microlite abundances and compositions, irrespective of proximal or distal location from the central vent (Supp Fig. 1). Clasts representative of vesicular scoria (Cole *et al.,* this volume) were selected for CSD. This has allowed us to compare differences in microlite size and shape as the eruption progressed, to understand the changing conditions, and determine whether future detailed CSD study may yield additional insights.

Crystal size distribution (CSD) and shapes of plagioclase

Changing conditions of ascent, including rate, growth style, and crystallinity, can be inferred from the slope and intercept of CSD curves and calculated crystal shapes. The CSD curves were generated for microphenocrysts and microlites, the crystals with lengths <100 µm (Supplementary Table S7). CSD curves for the lava dome, U1, U2, and U5 are presented with respect to the long axis of the crystal to document the size distributions of these small crystal populations (Fig. 9). Based on a tabular crystal morphology (typical for U1 crystals as described below), crystals with lengths <20 µm would have widths <5 µm and thus be too small for EMPA analysis. Therefore, a significant fraction of the crystals in the CSD analysis lack quantitative compositional data. However, some qualitative statements can be made about this population drawing on crystals that could be analysed that have similar comparative brightness in BSE images and elemental maps (Fig. 8).

The dome sample CSD has peaks at <1 µm and ~4 µm indicating the prevalence of very small microlites and possibly nanolites. The U1 CSD features an even larger population of small microlites (~5 µm), but has a second peak at ~50 µm. These two peaks and different slopes suggest that there are at least two populations of crystals that may have experienced different growth histories in U1.

The smallest crystal-size population has a high areal number density and feldspar microlite crystallinity (Table 2) and low median crystal area (1.97 μm^2). U2 and U5 are both distinct from U1 in that they have shallower slopes and lower population densities of the smallest crystals (long axes < 15 µm). The U2 CSD has a subtle inflection point at 20 µm suggesting the same two microlite – microphenocryst populations as U1, but with different proportions. The geometry of the curves for both U2 and U5 suggest their recorded growth and stagnation processes are more similar to each other than to U1. U2 appears to be transitional between U1 and U5, with an intermediate population density at the smallest microlite long axes.

The shape of the plagioclase crystals is presented in a Zingg plot of the aspect ratios generated by ShapeCalc (Fig. 9 inset) for all crystal sizes analyzed and offers complementary information to the CSD analysis. Although there may be some minor variation in shape with respect to crystal size in an individual sample, utilizing different bins did not affect the overall shape patterns observed. Dome microlites occur as bladed crystals. U1 and U2 have a more tabular average morphology, but appear similar to each other. However, U2 has fewer of the < 5 µm width, tabular microlites and a greater number of the larger microlites (including bladed crystals and zoned microlites), but fewer of the bladed, zoned microphenocrysts. These heterogeneities in crystal shape were apparent when fitting the U2 crystal shapes to known population groups (Mangler *et al.*, 2022) that were not as good a fit (r^2 =0.9678) as for U1, perhaps reflecting slightly different growth histories in U2. For U5, crystal shapes tend towards bladed, but are influenced by a minor more acicular population, which is typically associated with increasing undercooling (Shea and Hammer 2013). While a small proportion of the U5 microlite population is comprised of the smallest tabular group, these are by far the minority, which is also indicated by the CSD curve. Apparent low microlite crystallinity in BSE images from U5 are confirmed by the low areal number density (Table 2 and CSD curve) of feldspar microlites. However, the median crystal size is also the largest (9.69 μm^2 vs 1.97 μm^2 and 4.61 μm^2 for U1 and U2 respectively).

Variations in microlite population compositions

Microlites that could accommodate a beam width of > 5 microns (20 µm length) were analyzed and the total population of these microphenocrysts and microlites span ~50 mol% anorthite in composition, which broadly overlaps with the phenocrysts, but extends to more albitic compositions (An_{44}). Like the phenocrysts, the microlites occur as two distinct types: unzoned and simple normally zoned crystals, with unzoned crystals typically <An_{70} (Fig. 10). Although the largest crystals (microphenocrysts) are invariably zoned, there is not a strong trend between anorthite content and size amongst crystals analysed (Fig. 10), with a significant fraction of smaller crystals

displaying normal zoning. This could be a function of the orientation and 2D slice through the crystals. The crystals too small to be analyzed by EMPA are all unzoned but, based on comparative brightness in BSE, appear to have a similar (or more albitic; $<An_{45}$) composition to both the analysed unzoned microlites and the rims of zoned microlites.

Although the absolute range in plagioclase microlite composition is similar throughout the explosive eruptions, U1 has a distinctive microlite abundance, size distribution and phase compositions. Scoria from U1 has the highest groundmass crystallinity (36%), and features extensive microlite and microphenocryst crystallization. U1 plagioclase microlites analysed are dominated by zoned crystals, with cores ranging from An_{48} to $An_{93,}$ with the majority $>An_{70}$ (Fig. 11). The unzoned microlites showed a slightly more restricted composition, An_{46} to $An_{81,}$ with a mode ~$An_{65.}$. The rims of the zoned crystals were mostly too thin to analyze, but have a similar compositional range to the majority of the unzoned plagioclase microlites. U2-U5 have relatively fewer zoned An-rich microlites ($>An_{70}$; Fig 11). Like U1, the rim composition of the zoned plagioclase microlites (An_{47-74}) in U2-U5 is similar to the composition of the unzoned plagioclase microlites (An_{44-81}; Fig. 11), which is suggestive of a common origin.

The concentration of minor elements in the plagioclase microlites is distinctive, both between the units, between types of plagioclase (zoned vs. unzoned) and compared to phenocrysts (Fig. 6a). Overall, the concentrations of FeO and TiO_2 are higher in microlites compared to their concentrations in phenocrysts of the same anorthite content. The unzoned microlites have the highest FeO and TiO_2. Overall, the more sodic microlites contain higher FeO.

Olivine microlites generally span a similar range in forsterite content (Fo_{62-79}; median Fo_{74}) compared to the phenocrysts (Fig. 6b) and this does not vary as the eruption progresses (Fig. 11). However, olivine microlite abundance lowers significantly from U1 to the later phases of the eruption. Olivine represents nearly 45% of the mafic microlites (olivine + pyroxene + oxides) in U1, becoming only 12-19% in U2-U5 samples (Table 3). In all samples, the olivine microlite size exceeds 5 µm, and are absent in the smaller mafic microlite population, (Fig. 8f; S1). In one sample from unit U2, several of the olivine microlites are Fo-poor ($<Fo_{58}$) and armored by pyroxenes and oxides, but these are considered outliers. With respect to minor elements, the microlites average slightly higher CaO (Fig. 6b) and MnO concentrations, and lower NiO abundances than comparable phenocrysts. U1 olivines are slightly more enriched in CaO compared to the U2-U5 olivines (Fig 6b).

Pyroxene microlites are less common in U1 (~20% of mafic microlites), becoming more abundant in later phases of the eruption (45-57% of mafic microlites; Table 3).

Orthopyroxene/pigeonite (<Wo_{12}) microlite compositions are similar throughout the eruption, ranging from Mg# 59-74. Clinopyroxene microlites range from Mg# 67-89, with U1 encompassing almost the entire range. As the eruption progress, compositions of cpx appear to become more restricted (Mg# 73-83). However, the greatest difference between the eruptive phases is the appearance of intermediate composition pyroxenes (Wo_{12-38} or 6-18 wt% CaO) in U2-U5 that are not present in U1 (or the lava dome), as seen in Fig. 6c and Fig. 12. The broad range in Wo content (12-38 mol%) would classify the intermediate pyroxenes as pigeonite (at higher temperatures) and sub-calcic augite to augite. They do not plot on a single isotherm/solvus when the graphical thermometer of Lindsley (1983) is used (Fig. 6c) and thus may represent a disequilibrium phase. In addition to lacking the intermediate pyroxenes, U1's distinctive clinopyroxenes have >6 wt% Al_2O_3. Relative proportions of pyroxene varies with successive eruptions. In U1, cpx is twice as abundant as opx (Table 3). In U2-U5, the cpx proportion increases slightly as the eruption progresses, up to ~20%. Opx abundance varies more widely and the intermediate pyroxenes are most common in U2 and U3, decreasing in U5 (Table 3).

Titanomagnetite microlites in the scoria display no zoning or exsolution, but span a wider compositional range than the phenocrysts (Fig. 6d). U1 titanomagnetite microlites have lower Ti and Mn (Usp fraction 0.40-0.48) than any other microlites (Usp fraction 0.42-0.53) or the phenocrysts. U2-U5 titanomagnetite microlites trend towards higher Ti and Mn relative to the phenocrysts. With respect to minor components, MgO in titanomagnetite varies from 1-4 wt% across the eruptive sequence, whereas as Al_2O_3 appears to be a function of eruptive phase. Al_2O_3 is most enriched in U1, ranging from 2.5-4.9 wt%, whereas U3 spans a lower, narrower range (1.9-2.4 wt%). Titanomagnetite from U2 and U5 have intermediate Al_2O_3 concentrations (1.9-3.8 wt%). Although the relative abundances of olivine and pyroxenes varies during the eruption, titanomagnetite proportions show little change (31-38% of mafic phases) and crystal sizes range across the microlite size distribution (Fig. 8f).

Dome microlites

The microlite phase assemblage and textures in the lava dome are unique compared to the explosive phases. The plagioclase microlites are dominated (>80%) by an unzoned, more albitic population (An_{42-57}), with relatively few zoned or more An-rich microlites (Fig. 11). The cores of the zoned crystals vary from An_{51-91}, with a restricted rim composition (An_{42-54}), that matches the unzoned microlite composition in the dome. Olivine microlites are not present and clinopyroxene microlites are rare and very small, found mostly along vesicle edges. Orthopyroxene (Mg# 58-74) is the dominant mafic microlite, comprising ~95% of the pyroxene population. Titanomagnetite

microlites (Usp fraction 0.41-0.55) in the dome are ubiquitous and span a greater compositional range than in any other unit, with clear evidence of exsolution (Fig. 6d) and do not conform to the tight linear Mn-Ti trend observed in the scoria phenocrysts and microlites. They are depleted in Al_2O_3 (<2 wt%) with respect to the titanomagnetite in the scoria. At the analyzable scale (>5 μm), the oxides comprise ~30% of the mafic phases (Table 3) which is similar to the proportions observed in the scoria. However, very small titanomagnetites are much more abundant in the dome than scoria (Table 2). The very small oxides are particularly prevalent in reaction textures around pyroxene microlites, which is a texture unique to the lava dome (Fig. 8a).

Summary change in microlites as eruption progresses

The lava dome groundmass is characterized by reaction textures and an abundance of unzoned, An-poor plagioclase and orthopyroxene, with extensive crystallization of microlites <5 μm. The explosive phases appear to have at least two different populations of microlites within any one sample. U1 has the most crystalline groundmass (36%), with crystals <5 μm (width) particularly abundant. The analyzable U1 microlite phase assemblage is dominated by normally zoned calcic plagioclase and olivine, with minor clinopyroxene and titanomagnetite, but by far the most abundant microlite phase is the <5 um width, tabular, low-An microlites. These smaller microlites reflect a nucleation-dominated history, whereas the larger microlites/microphenocrysts are growth-dominated. Nucleation-dominated growth is characterized by abundant small crystals, whereas growth-dominated crystallization produces fewer, larger crystals, as more extensive crystallization is inhibited by a lack of nucleation sites. In successive units (U2-U5), groundmass crystallinity decreases (by 5-10%), as does of the proportion of high-An zoned plagioclase and olivine in the assemblage (Fig. 11). The relative abundance of pyroxene increases in U2-U5, with the emergence of a disequilibrium intermediate phase (Wo_{12-38}) in addition to cpx and opx. Within all units, the unzoned plagioclase microlites and the rims of the zoned plagioclase microlites are relatively An-poor ($An_{45-65;}$ Fig. 10, Fig. 11). Plagioclase microlite shapes transition from tabular (U1-U2) to more bladed (with some acicular) in U5. The change in the microlite compositions, crystallinity, and morphology is accompanied by a change in vesicularity as the eruption progressed. Median bubble size in U1 is approximately half that of U2, reflecting an increasing bubble size as the eruption progressed. The analyzed clast from U5 has the highest vesicularity (51%), lowest bubble number density (77) and highest median vesicle area (252 μm^2) and bubbles show increased evidence of coalescence (Cole *et al.* this volume; Christopher *et al.* this volume).

Assessment of equilibrium

Although the phenocrysts and microlites do not show obvious textural signs of disequilibrium (e.g. reverse zoning, resorption, embayments, coronas), chemical equilibrium between phases and the host melt must be assessed to ensure the applicability of any thermometers, barometers, or hygrometers. Weber *et al.* (this volume) explore the equilibrium of pyroxene and plagioclase phenocrysts and concluded that a significant proportion of the phenocryst population appears to be antecrystic and likely represent 'recycled' crystals from previous/eruptive crystallization events.

Most microlites typically form as a result of decompression-induced crystallization upon ascent and represent the final crystallization of a magma prior to eruption. However, microlites can also be antecrystic, for example incorporated from a more mafic source, as documented by Martel et al. (2006) for Mt. Pelée, Martinique and Humphreys et al. (2009) for Soufrière Hills, Montserrat. In the La Soufrière scoria, there are at least two populations of microlites (zoned plagioclase + olivine + cpx + ttm; unzoned plagioclase + cpx + opx + int. pyx + ttm) and we calculated various mineral-melt K_Ds as a potential assessment of equilibrium. The generally accepted K_Ds of the various mineral phases with respect to liquid are:

$K_D(An–Ab)^{plg–liq} = 0.10 \pm 0.05$ at T <1050˚C (Putirka, 2008)

$K_D(Fe^{2+}–Mg)^{opx–liq} = 0.29 \pm 0.06$ (Putirka, 2008)

$K_D(Fe^{2+}–Mg)^{cpx–liq} = 0.28 \pm 0.08$ (Putirka, 2008)

$K_D(Fe^{2+}–Mg)^{ol–liq} = 0.3 \pm 0.03$ (Roeder and Emslie 1970)

Using the exchange coefficient approach on the microlites in the explosive deposits, only 31% of the plagioclase, 81% of the opx, 54% of the cpx, and 18% of the olivine microlites fall *within* the accepted K_D parameters of equilibrium with the andesitic carrier melt (Supplemental Fig. 3) proposed by Weber *et al.* (this volume). Thus, the vast majority of plagioclase and olivine, as well as about half of the cpx are likely not in equilibrium with the carrier melt based on K_D. Although the carrier melt is not one fixed composition nonetheless the broad range of microlite compositions suggests that equilibrium is unlikely, as described below.

We also recognize that equilibrium K_Ds should be approached with caution and that equilibrium conditions cannot be assumed *a priori* based on the exchange reaction value. For example, Humphreys *et al.* (2016) demonstrated that both temperature and K_D are affected by decompression rate and that growth of the equilibrium feldspar composition becomes impeded during H_2O degassing as melt viscosity and species diffusivities increase. Thus, in hydrous systems

such as subduction zones where degassing-induced crystallization is prominent, calculated plagioclase-melt K_Ds should be used with caution and may not be sufficient to indicate complete equilibration. Melekhova *et al.* (2015) similarly cautioned against the assumption of equilibrium for olivine-melt K_Ds in the "accepted" range of 0.3 $\pm$ 0.03, as iron is typically measured as Fe^{2+}, when there may be a significant Fe^{3+} component, particularly in oxidized melts typical of arcs. The $^{Fe\text{-}Mg}K_D$ exchange coefficients of pyroxenes-melt would be similarly affected.

A complementary approach to assess equilibrium between phase and melt is to compare the mineral compositions measured in the erupted samples in this study to experimental mineral compositions, where intensive variables are well known and constrained (Waters *et al.* 2021). Based on this comparison, we can assess whether the microlites could have plausibly grown from the hypothesized carrier melt-composition derived from the groundmass melt analyses. In Fig. 13a, we show the range of plagioclase compositions from the natural samples with plagioclase-liquid pairs from hydrous, fluid-undersaturated, mixed volatile (H_2O–CO_2), and anhydrous phase equilibrium experiments, as compiled from the literature by Waters *et al.* (2021). Here, we have used the carrier melt estimates in Weber *et al.* (this volume) to illustrate a plausible range for the natural liquid compositions. The more An-rich plagioclase microlites more closely correspond with the hydrous experiments, owing to the effect of H_2O on stabilizing a more calcic plagioclase composition (Housh and Luhr 1991; Sisson and Grove 1993; Panjasawatwong *et al.* 1995; Lange *et al.* 2009).. The plagioclase compositions from the unzoned microlites and the rims of the zoned microlites in the 2021 La Soufrière explosive deposits overlap with the compositions of experimental equilibrated plagioclase in both anhydrous and hydrous andesite-dacite melts. However, no experiments from this compositional range produce An-rich plagioclase (>An_{76}), which is the predominant composition observed in microlite cores from this eruption. The lack of overlap between the cores and experimental plagioclase-liquidus pairs suggests that the microlite cores have a separate and distinct origin compared to the unzoned microlites and the microlite rims, as explored in the discussion.

The orthopyroxene and clinopyroxene microlites from La Soufrière are also compared to the pyx-liquid pairs in the experimental literature (Waters *et al.* 2021). For the experimental dataset, the liquid Mg-numbers were obtained by recalculating the ferrous iron content of the liquids co-existing with the orthopyroxene crystals using Kress and Carmichael (1991). All FeO was considered to be ferrous in the pyroxene compositions. The lower Mg-number orthopyroxene microlites overlap with the experimentally grown orthopyroxenes, but higher Mg-number microlites are beyond the experimental range (Fig. 13b). This is consistent with the low K_D Fe-Mg exchange calculation for opx-liquid (phenocrysts) noted by Weber et al. (this volume). Similarly, a significant portion of the

clinopyroxene microlite data does not overlap with the majority of experimentally grown clinopyroxene in andesite-dacite melts (Fig. 13c). The U1 microlites are more Mg-rich than those in U2-U5, and thus further from the experimental cpx compositions. Interestingly, there are a few outliers in the experimental dataset, with a relatively low liquid Mg-number and high Mg-number cpx from Blatter and Carmichael (1998) and Martel *et al.* (1999) that are in a similar compositional space to the U1 microlites.

Based on comparison with the experimental literature, there is a population of unzoned plagioclase and less Mg-rich opx and cpx microlites that could have crystallized upon ascent from the andesitic carrier liquid. However, a second population of microlites falls outside the experimental data set ranges (plagioclase >An_{76}; cpx >Mg#70; opx >Mg#65), which matches our conclusions based on the K_D calculations. The non-equilibrium population (high-An plag + ol + cpx) is inferred to be older and inherited, likely recording pre-eruptive stalling and crystallization. This inherited population is dominant in the initial U1 explosive phase, but becomes scarcer as the eruption progresses. We explore this further in the discussion.

Estimating water from hygrometry and phase equilibrium experiments

Although broad ranges in plagioclase composition may be the result of magma mixing and crystal entrainment, up to 40 mol% variation in anorthite content may be a consequence of changing water content as magma ascends and degasses (Frey and Lange 2011). To assess whether volatiles could be playing a role in mineral compositional variation at La Soufrière, plagioclase hygrometry and phase equilibrium experiments are considered. Recent plagioclase hygrometers (e.g. Lange *et al.* 2009; Waters and Lange 2015) are thermodynamic models based on the plagioclase-liquid exchange reaction between anorthite and albite components, calibrated on plagioclase-liquid experiments. The models allow us to estimate the dissolved water content in a melt if temperature, pressure, the composition of plagioclase crystals, and melt from which they grew are known. Applying the plagioclase hygrometer to the 2021 La Soufrière scoria samples a significant proportion of the crystal cargo is not in equilibrium with the host-liquid, which itself fixed in composition. This complicates use of the plagioclase hygrometer. Nonetheless, we can use that and published phase-equilibrium experiments to make some broad generalizations about the likely dissolved water content during the explosive eruption, and to infer magmatic conditions prior to the explosive behavior.

Owing to the complexity of the crystal cargo, Weber *et al.* (this volume) explored several different thermometers and barometers using a range of possible groundmass compositions and determined that the most likely PT conditions for phenocrysts that formed in the andesitic carrier

melt were ~1000˚C and 2-3 kbars. Using these inputs in conjunction with the groundmass compositional range (~64 wt% SiO_2) and the composition of unzoned plagioclase microlites or the rims of plagioclase microlites (An_{46-68}) that are plausibly in equilibrium with the host melt (Fig. 13) yields a range of water contents of 2.8-3.1 wt%. Previous studies of melt inclusions in olivine from St. Vincent basalts recovered 0.8-5.2 wt% H_2O (Bouvier *et al.* 2008), whereas recently analyzed melt inclusions from various mineral phases in the 2021 eruptive event were slightly more restricted and ranged from 1.5 to 3.9 wt.% H_2O (Weber *et al*., this volume). Analyses of groundmass glass in U1-U3 generated analytical totals ~97%. Thus, the amount of dissolved water in the magma system when the unzoned plagioclase microlites (and microlite rims) crystallized is consistent with other independent estimates of water in the system.

In contrast, comparison with phase-equilibrium experiments (Fig. 13a), suggests the cores of many zoned microlites are too calcic to have formed from the andesitic carrier melt and likely crystallized in a more mafic and/or wetter magma. Other studies in the Lesser Antilles have also noted calcic microlites and proposed mechanisms for their origin. Martel *et al.* (2006) used phase equilibrium experiments to demonstrate that calcic plagioclase microlites (>An_{70}) in andesitic deposits from Mt. Pelée (Martinique) could not have formed upon magma ascent, but grew in a pre-eruptive mafic (basaltic) magma with at least 6.5-8.5 wt% dissolved H_2O. That study complemented earlier basaltic andesite Pelée experiments at 4 kbar which showed that plagioclase compositions >An_{85} typically require >5 wt% H_2O at temperatures of 1025°C (Martel et al., 1999).

Discussion

Element partitioning in minerals

Phenocryst compositions are often distinct from the microlite compositions, and within the microlites there are distinctions between the dome microlites, U1, and the U2-U5 microlites (Figure 6). The differences in element partitioning of various minerals, can place some constraints on the microlite origins for various stages of the eruption.

The plagioclase microlites show negative correlations between FeO and anorthite at higher and lower An concentrations (Fig. 6a). Similar trends are observed in MgO and TiO_2 with anorthite. Bindeman *et al.* (1998) showed experimentally that there is an increase in Fe partitioning with decreasing anorthite content and noted that oxygen fugacity could play a role. Kinetic effects could also explain an increase in Fe if crystal growth rates outpace diffusion. Bacon (1989) demonstrated that for incompatible elements like Fe, a boundary layer (enriched by 30-50%) may form around the crystal, resulting in enrichment in the crystal. Thus, the Fe-enrichment trend observed in the low-An

microlites is consistent with local rapid growth and kinetic control and the nucleation dominated crystallization inferred from the CSD analysis. It is possible that the high-An trend observed in the cores of the microlites and phenocrysts also reflects a kinetic control. Other experiments demonstrate that partitioning coefficients change with cooling rate, with relative increases in Fe, Mg, Ca, and Al with increasing An (Mollo *et al.* 2011). However, this trend was not observed in the La Soufriere microlites, suggesting that changes in cooling rate are likely not driving the compositional variation observed. A magma mixing origin is also not plausible to explain the high-An plagioclase microlites at La Soufrière, unlike at the Soufriere Hills (Humphreys *et al.* 2009) or Mt. Pelée (Martel *et al.* 2006), as the Fe concentration in the calcic microlites does not display a positive correlation with increasing An.

The U2-U5 eruptions uniquely have three pyroxene microlite compositions, including an intermediate Wo component (Wo_{12-38}; pigeonite and sub-calcic augite), but not observed in the dome and U1 samples (Fig. 6c). The preservation of pigeonite is consistent with high temperature crystallization and rapid cooling, as it breaks down outside its thermal stability field during slow cooling. It may also be suggestive of more reducing conditions, as orthopyroxene becomes the stable low-Ca pyroxene phase at oxygen fugacities >Ni-NiO (Grove and Juster 1989). As a group, the intermediate pyx from U2-U5 do not plot on a single isotherm or solvus on the graphical thermometer of Lindsley (1983), which is likely a consequence of disequilibrium crystallization due to undercooling during rapid ascent. These intermediate composition pyroxene crystals are notably absent in the initial U1 phase of the eruption, which is inferred to have ascended more slowly based on CSD analysis and greater extent of groundmass crystallization. Given the resolution of our BSE images and elemental maps from the SEM, these intermediate pyx are texturally indistinguishable from the average-CaO (Wo_{40-48}) cpx and occur with opx and cpx. However, transmission electron microscopy (TEM) could reveal that the intermediate pyroxenes are composite mixtures comprised of domains of orthopyroxene, augite, and sub-calcic augite, as observed in studies of pyroxene nanolites (Mujin *et al.* 2017). This could be the focus of further study.

The Ti concentration in the titanomagnetites is higher in the U2-U5 microlites than the U1 microlites (Fig. 6d). Higher Ti abundances have been correlated with higher temperatures and lower oxygen fugacities (Frost and Lindsley 1991; Devine *et al.* 2003). A higher temperature origin for the U2-U5 titanomagnetite microlites would be consistent with the higher temperatures inferred from the intermediate composition pyroxenes in U2-U5. The dome titanomagnetite microlites have both higher and lower Ti concentrations, attributed to exsolution and/or different crystallization conditions. Element partitioning (e.g. Ti, Al, Mg) into titanomagnetite has also been shown to be a

function of cooling rate, as demonstrated by experiments on trachybasalt from Mt. Etna (Mollo *et al.* 2013); at higher cooling rates, titanomagnetite is enriched in Al and Mg and depleted in Ti, as crystals have not had sufficient time to re-equilibrate with the melt. Interestingly, the U1 titanomagnetites have the lowest Ti and highest Al concentrations (and lowest ulvospinel fraction), which would be consistent with the fastest cooling rate. However, unlike in the Mt. Etna experiments, there does not appear to be a correlation between Al and Mg, with each eruptive phase displaying a range of Mg in titanomagnetite. Therefore, an increase in temperature is a more plausible explanation for the compositional differences observed. This is further supported by the lack of any rapid-growth dendritic textures in the titanomagnetites in any of the eruptive phases.

Origin of various microlite populations

The lava dome microlite assemblage of low-An plag (An_{45-60}), orthopyroxene, and titanomagnetite is distinctive compared to the microlites in the scoria and is likely not related to the explosive sequence. The plagioclase microlites are more sodic than in the explosive units (Fig. 11), orthopyroxene is the dominant mafic phase (Table 3), the titanomagnetite is exsolved (Fig. 6d) and the shape of the dome CSD curve is different (Fig. 9). To constrain the origin of the dome microlites, a possible andesitic analog from western Mexico (62 wt% SiO_2) is considered, in which water-saturated phase equilibrium experiments were run under a nickel-nickel oxide oxygen buffer. The experiments suggest that an assemblage of plag + opx + ttm would be restricted to P (H_2O) < 300 bars (<2 wt% H_2O) at temperatures ~1125˚C, with augite joining the assemblage as temperature decreased (Moore and Carmichael 1998). If these results can be applied to the 2021 lava dome, it would suggest that the dome microlites formed at very shallow levels in the crust and were mostly degassed/dry, which is in stark contrast to the microlites in the scoria. In recent 1 atm experiments on samples from the 2021 eruption, the microlite phase assemblage, compositions, and textures of the lava dome were favorably reproduced at conditions of 900˚C and Ni-NiO +2. The plagioclase was An_{48-54} and opx showed some breakdown textures, which became more pronounced at more oxidizing conditions (Morrison Evans *et al.* this volume). Given the lack of a genetic relationship with the scoria samples, it is plausible that the lava dome is actually degassed magma from a prior eruption (e.g., 1979, 1971) that has been rejuvenated and pushed to the surface, as proposed by Joseph *et al*. (2022 and Sparks *et al* (this volume).

The microlites in the scoria appear to reflect at least two different origins. The normally zoned plagioclase microlites with An-rich cores are most abundant in scoria from U1, as are olivine microlites (Fo_{63-79}), suggesting that they likely crystallized together. These are also the portion of the microlite phases that are not in equilibrium with an andesitic carrier melt, based on both K_{Ds} and

comparison to experimental studies. High-An plagioclase and co-existing low-Fo olivine in basalt/basaltic-andesite melts has been shown to be a consequence of suppression of the albite component in plagioclase by high water content (Sisson and Grove 1993). In St. Vincent, this assemblage was previously observed in cumulates and a model was proposed for early crystallization of olivine and Cr-rich spinel from primitive hydrous high-Mg basalts that subsequently ascended rapidly. This differentiated melt stalled at shallow depths where water saturation was reached and plagioclase (high-An) and olivine (low-Fo) subsequently crystallized (Tollan *et al.* 2012). Melehkova *et al.* (2015) explored St. Vincent cumulates further and found that An-rich plagioclase and evolved olivine could only be reproduced experimentally under water-saturated conditions at 4 kbars and 1050˚C. Thus, the microlites in U1 that are out of equilibrium with an andesitic carrier melt were likely derived from a H_2O-rich mafic melt that had undergone significant differentiation and crystallized at ~15 km depth. In addition to the plagioclase and olivine, clinopyroxene and titanomagnetite likely crystallized, as much of the cpx is out of equilibrium with the carrier melt and the titanomagnetite in U1 was distinctive compared to the other units (Fig. 6d). This "inherited" microlite population dominates the analyzable U1 scoria, but a second population of microlites is also present in U1. The U1 CSD has a clear peak ~50 um representing the zoned microphenocrysts of the inherited microlites, and a second peak at 5 um, capturing the unzoned smallest An-poor ($<An_{55}$) microlites, many of which were too small to be analyzed (Fig. 9). These An-poor microlites are in equilibrium with the carrier melt and likely formed upon ascent, as did the rims of the inherited microlites, which are the same An-poor composition (Fig. 11). Many of the olivine microlites also feature very thin, more Fe-rich rims which likely grew during ascent, as the olivine was attempting to equilibrate with the carrier melt.

Given the change in the microlite assemblage after the initial series of U1 eruptions during the first ~21 hours, a different P-T-XH2O pathway for the creation of U2-U5 microlites must be considered. The U2-U5 microlites are characterized by high-Fe/low-An plagioclase, intermediate pyroxenes and the higher-Ti titanomagnetite, which contrast with the dominant U1 microlite assemblage (Fig. 6). The U2-U5 microlites likely formed from a slightly different (possibly more evolved) magma batch or melt lenses than U1, that experienced higher temperatures or rate of undercooling. The higher temperatures could be a consequence of latent heat released during decompression (Blundy *et al.* 2006). This second microlite population is in equilibrium with its carrier melt and these microlites are thus considered syn-eruptive or "juvenile", likely forming upon ascent. Notably, this microlite assemblage was subordinate until after the initial explosions, evacuation of the conduit, and removal of the lava dome, allowing for a more direct magma connection to the surface, as discussed in the next section. The U2-U5 eruptions appear to contain a mixture of

inherited and juvenile microlites, as microlites characteristic of the U1 microlite assemblage (normally zoned plagioclase and olivine) are present in all phases, but diminish as the eruption progresses. The CSD for U2 has an inflection point at ~20 um, consistent with a mixed population, but a similar trend is not observed in U5 (Fig. 9). The U5 eruptions therefore may have little remnant of the U1 assemblage, as also supported by the relative abundance of mafic phases (Table 3).

Linking petrology, geophysical monitoring and eruptive stratigraphy

Our detailed, stratigraphically constrained microlite analysis allows us to have insights into what processes were occurring in the magmatic system in the lead-up to and during the explosive sequence at La Soufrière. In Fig. 14, we attempt to place the different microlite populations in context with the various eruptive units and relate their origins to measured geophysical parameters over the course of the volcanic unrest and crisis. The petrological evidence suggests that despite the near ubiquitous presence of similar phenocryst assemblages, the 2020-2021 La Soufrière eruption was made up of several discrete batches of magma, possibly with a reasonably similar point of origin that accessed pre-existing phenocrysts and melt, but which underwent different stages of ascent and stalling prior to eruption. The microlite assemblage, compositional, and CSD data suggests that there were three such batches. Batch 1 is comprised of the low-An plagioclase (An_{45-60}), orthopyroxene, and titanomagnetite microlites (observed in the dome). Batch 2 is comprised of high-An plagioclase (>An_{75}), olivine, clinopyroxene, and titanomagnetite microlites. Batch 2 is the dominant melt in U1, but also present in U2-U5. Batch 3 is comprised of moderate An plagioclase (An_{50-75}), clinopyroxene, orthopyroxene, intermediate pyroxene, and titanomagnetite microlites. The batch 3 assemblage is found in U2-U5 and is the dominant assemblage in U5.

There are several strands of evidence that point to the initial dome (sampled in mid-January 2021) being largely composed of re-invigorated melt/mush that may have been substantially degassed and cooled slowly at shallow depths. Compared to the scoria, it includes a unique microlite assemblage (low-An plagioclase + orthopyroxene + titanomagnetite), altered mafic microlites, exsolved titanomagnetite, and reaction margins on mafic phenocrysts (olivine and pyroxene) (Fig. 8a). This assemblage is melt batch 1 in our model (Fig. 14a). Annealed fluid pathways, as well as precipitation of pyrite, suggest interaction with hydrothermal fluids at shallow levels. These observations are consistent with the rheological model developed by Sparks *et al.* (this volume) who suggested that a degassed, partially crystalline magma from previous eruptions was extruded by a volatile-rich magma ascending from depth. Our petrologic data suggests that the explosive eruptions were derived from a wet melt, but the trigger for the effusive phase remains enigmatic based on our petrologic analysis.

We can use the other monitoring data to suggest time constraints for the movement and growth phases of these melts. After months of low-level seismicity, the earthquake behavior at La Soufrière changed, with a swarm of relatively shallow (~5km) VT earthquakes on 23-24 March, 2021, thought to be associated with the movement of fluids. The VT swarm was accompanied by an increase in CO_2 (Joseph *et al.* 2022), which is typically indicative of more deeply sourced magma. These physical changes in unrest behavior may be the manifestation of the injection of a new pulse of magma from depth and the subsequent onset of microlite crystallization and degassing. In our model, we suggest the fluid pulse and associated unrest recorded then is generated by melt batch 2, which is characterized by high-An plagioclase (>An_{75}), olivine, clinopyroxene, and titanomagnetite. The depth of crystallization is constrained by the high-An plagioclase + low-Fo olivine compositions, which have been experimentally reproduced at ~4 kbars from a water-saturated mafic melt (Melekhova *et al.* 2015). The relatively deep storage depth is broadly consistent with the water saturation depth of a wet magma, as modeled by Rasmussen *et al.* (2022), as well as the deformation depths at La Soufriere (~18 km) as modeled by Camejo-Harry *et al.* (this volume). Once mafic melts reach H_2O saturation, degassing induced crystallization increases the magma viscosity and promotes stalling, forming a more evolved melt (Zellmer *et al.* 2016). Over the next two weeks, the microlites continued to crystallize.

A deeper swarm of VT earthquakes, located at ~10 km, were recorded on 5th April, just four days prior to the explosions and has been interpreted as a new volume of magma ascending from depth (Joseph *et al.* 2022). We believe this to be an expression of second boiling of the stalled magma and migration of fluids, as the two-week microlite crystallization episode concentrated the volatiles in the melt leading to saturation. The subsequent exsolution initiated the ascent of magma batch 2, and the crystallization of a second microlite population (plagioclase <An_{65} + clinopyroxene + orthopyroxene + titanomagnetite) and rims on the inherited microlites (Fig. 14). The slow ascent to the surface allowed extensive microlite crystallization (22%) which changed the magma's rheology and increased viscosity. Lindoo *et al.* (2017) demonstrated that for a basaltic andesite, 20% microlite crystallization is a critical threshold for establishing yield strength and decreasing permeability. Rapid microlite crystallization in basalts may induce fragmentation, as shown in experiments and numerical models (Moitra *et al.* 2018; Arzilli *et al.* 2019), potentially leading to explosive eruption.

Up to two days prior to the explosive eruptions, the rate of dome growth increased significantly based on camera and inSAR observations (Stinton *et al.* this volume; Dualeh *et al.* 2023), and on the 8th of April weak SO_2 plume was detected (Joseph *et al*. 2022). This suggests the batch 2 magma had risen to shallow depths, beginning to accelerate as vesiculation increased. Up to that

point, the extensive microlite crystallization of batch 2 may have inhibited significant exsolution and bubble growth, leading to overpressurization. During the months of lava dome effusion, very little SO_2 was detected and hydrothermal waters did not change composition (Christopher *et al*. this volume). Degassing in the crystal-rich batch 2 magma may have only been possible through fractured pathways and brittle failure, so the first explosions on 9th April acted as a vent clearing, erosive event. Prior to its final ascent, this magma had scavenged and entrained phenocrysts, glomercrysts, and xenocrysts, giving rise to the complex crystal cargo not in equilibrium with the carrier melt (Fig. 14). Similar entrainment of xenocrysts by ascending melts has been described in Dominica based on discrete age populations of zircons (Frey *et al.* 2018). Brittle failure in the initial explosive eruptions at La Soufrière is supported by the textures of the U1 scoria (e.g. shattered crystals), as well as the pulsatory nature of the U1 phase and lack of ash produced. The tephra deposits from the U1 explosive activity were characterized as lapilli-rich/ash poor and coarsened as the periodic blasts continued over the next 19 hours (Cole *et al.* this volume), destroying most of the 3-month old lava dome, the 1979 lava dome, and eroding the conduit.

After the initial U1 explosion, earthquakes deepened from ~3 to 5 km and another explosion didn't occur for six hours (Joseph *et al.* 2022). There was also a significant change in the deformation, with deep deflation (Joseph *et al.* 2022; Camejo-Harry *et al*. this volume) prior to the onset of the U2 activity on the morning of 10th April. The U2 explosive activity differed physically from the initial eruptions (Cole *et al*. this volume) and featured different proportions of the two microlite populations. In our model, the explosions associated with U2 are the first eruptions to tap magma batch 3. The final rapid ascent and eruption of U1/batch 2 led to subsequent decompression, allowing batch 3 to undergo decompression induced crystallization of microlites. The batch 3 melt contained microlites in equilibrium with the carrier melt (moderate An plagioclase (An_{50-75}), clinopyroxene, orthopyroxene, intermediate pyroxene, and titanomagnetite), as well as some of the inherited microlites from batch 2. We envision that batch 3 is incorporating these microlites, as well as glomerocrysts and xenocrysts during ascent and intermediate storage (Fig. 14). The U2 CSD profile has an inflection point at ~20 um, consistent with a mixed microlite population (Fig. 9). The profile also suggests faster ascent rates, which is corroborated by the lower measured crystallinity of the groundmass. The U2 sequence was ash-rich and the repose time between eruptions decreased, likely a consequence of repeated system pressurization, vesiculation, and failure (Cole *et al.* this volume and Sparks *et al.* this volume). The destruction of the overlying lava dome(s) and material in the conduit by the catastrophic U1 eruption(s) led to a more open-system and faster ascent of subsequent melts.

The eruption of U3 began late on 10th April and was marked by the onset of pyroclastic density currents and the fallout of coarse vesicular lapilli, as the vent/crater widened (Cole *et al.* this volume). Although the physical characteristics of the eruption changed and there are subtle changes in vesicle morphology and abundance, the groundmass microlite assemblage and composition is indistinguishable from U2. The data suggest that U3 is like U2, a mix of microlites from batch 3 and batch 2 melts.

The U5 sequence features more physical changes, including the lowest crystallinity and largest bubbles (Christopher *et al.* this volume), as well as the coarsest lapilli. The U5 eruptions had the fastest ascent rate, which inhibited the nucleation of crystals and led to more acicular morphologies amongst the microlites. Compared to U2 and U3, the quantity of the inherited microlites from batch 2 is diminished (Table 3) and the U5 CSD does not appear to reflect a mixed population and lacks small microlites (Fig 9), which would be consistent with rapid ascent as shown by Bernard and Bouvet de Maisonneuve (2020). In our model, U5 is predominantly composed of batch 3 melts freely vesiculating and rapidly ascending (Fig. 14). The evidence of batch 2 melts, which likely were responsible for the transition from effusive to explosive behavior, is largely absent from the tephra deposits <48 hours after the eruptions began.

Conclusions

This study demonstrates the importance of detailed analysis of microlites in stratigraphically well-constrained tephra sequences to elucidate what may drive changes in eruptive style and how it may be manifested in monitoring data. Although the phenocryst assemblage and whole-rock chemistry was virtually indistinguishable between the 2021 lava dome and explosive deposits (and most of the historic eruptions of La Soufrière), the groundmass crystallization was distinctive, allowing us to explore how an eruption not driven by a mafic injection may be initiated and evolve over a short period of time (<48 hours). For the last 500 years, La Soufriere has consistently erupted basaltic andesite (with the exception of the final March 1903 explosions from the 1902-03 sequence) and these eruptions have been attributed to a build-up of volatile pressure related to magma stalling at shallow levels of the crust (Fedele *et al.* 2021). Our microlite study supports that broad interpretation and offers additional constraints on syn-eruptive crystallization and rates of ascent, which are dynamic over short time-scales. The magmatic system beneath La Soufrière does not appear to be compositionally evolving over time, but may erupt in different styles based on level of overpressurization and availability of pathways for degassing and ascent. Eruptions within a single event (e.g., December 2020-April 2021) may be comprised of multiple discrete magma batches and crystals from the magma mush. Because these antecrysts are derived from compositionally similar

mushes and incorporated quickly into the ascending melts, they frequently lack any textural disequilibrium textures. However, assessment of chemical equilibrium and comparison with trace elements in microlites (Fig. 6) suggests that the majority of larger crystals are not syn-eruptive and should be used with caution to infer pre-eruptive conditions in the magmatic system. The phenocrysts may have crystallized during different episodes and been remobilized and are thus not a reliable indicator of pressure, temperature, or water content of the melt prior to eruption.

Given the complexity of microlite assemblages/compositions and groundmass textures documented for the recent period of activity at La Soufrière, additional quantitative groundmass analysis could provide more clarity on the effusive-explosive transition. Although we analyzed samples from four different explosive units and found trends to be consistent within vesicular scoria clasts from each unit, a more detailed study of the various clast types identified (Cole *et al*. this volume) would ensure that our samples were indeed representative. In particular, additional samples from the U1 phase should be considered, as its origin and ascent could be more closely linked with changes in seismicity and degassing in the weeks/days leading up to the 9th April, 2021 explosion. Our proposed model of eruption involves volatile oversaturation generated by second boiling, but a definitive trigger for the change in eruptive style remains somewhat enigmatic and other mechanisms such as CO_2 flushing could be more fully explored.

Acknowledgements

The authors are grateful to R. Robertson and the UWI Seismic Centre for discussion and support in the field. M. Jercinovic is thanked for help with electron microprobe analysis at UMass-Amherst. Reviews by Olivier Bernard, an anonymous reviewer, and editor Steve Sparks helped us to clarify and articulate our observations and interpretations.

Funding

This study was supported by the United States National Science Foundation (NSF) through Grants for Rapid Response Research (Award # 2132566) to H.F and M.M. J.B. B.V.D. and P.C. were supported by the UK Natural Environment Research Council (NERC) through an Urgency Grant (NE/W000725/1).

CRediT author statement

Holli Frey: Funding acquisition (PI), Conceptualization, Investigation, Visualization, Writing- Original draft, Project administration. **Matthew Manon:** Conceptualization, Investigation, Formal analysis, Data Curation, Software, Funding acquisition (co-PI), Writing- Review & Editing. **Jenni Barclay**:

Resources, Conceptualization, Investigation, Writing- Review & Editing. **Bridie Davis:** Investigation, Writing- Review & Editing. **Sydney Walters**: Investigation. **Paul Cole:** Resources, Conceptualization, Investigation, Writing- Review & Editing. **Thomas Christopher:** Resources, Investigation. **Erouscilla Joseph:** Resources, Writing- Review & Editing.

Data availability

All data generated or analyzed during this study are included in this published article (and its supplementary information files).

References

Arculus, R.J. and Wills, K.J.A. 1980. The Petrology of Plutonic Blocks and Inclusions from the Lesser Antilles Island Arc. *Journal of Petrology*, **21**, 743–799, https://doi.org/10.1093/petrology/21.4.743.

Arzilli, F., La Spina, G., et al. 2019. Magma fragmentation in highly explosive basaltic eruptions induced by rapid crystallization. *Nature Geoscience*, **12**, 1023–1028, https://doi.org/10.1038/s41561-019-0468-6.

Bacon, C.R. 1989. Crystallization of accessory phases in magmas by local saturation adjacent to phenocrysts. *Geochimica et Cosmochimica Acta*, **53**, 1055–1066, https://doi.org/10.1016/0016-7037(89)90210-X.

Bernard, O. and Bouvet de Maisonneuve, C. 2020. Controls on eruption style at Rabaul, Papua New Guinea – Insights from microlites, porosity and permeability measurements. *Journal of Volcanology and Geothermal Research*, **406**, 107068, https://doi.org/10.1016/j.jvolgeores.2020.107068.

Bindeman, I.N., Davis, A.M. and Drake, M.J. 1998. Ion Microprobe Study of Plagioclase-Basalt Partition Experiments at Natural Concentration Levels of Trace Elements. *Geochimica et Cosmochimica Acta*, **62**, 1175–1193, https://doi.org/10.1016/S0016-7037(98)00047-7.

Blatter, D.L. and Carmichael, I.S.E. 1998. Plagioclase-free andesites from Zitácuaro (Michoacán), Mexico: petrology and experimental constraints. *Contributions to Mineralogy and Petrology*, **132**, 121–138, https://doi.org/10.1007/s004100050411.

Blundy, J., Cashman, K. and Humphreys, M. 2006. Magma heating by decompression-driven crystallization beneath andesite volcanoes. *Nature*, **443**, 76–80, https://doi.org/10.1038/nature05100.

Bouvier, A.-S., Métrich, N. and Deloule, E. 2008. Slab-Derived Fluids in the Magma Sources of St. Vincent (Lesser Antilles Arc): Volatile and Light Element Imprints. *Journal of Petrology*, **49**, 1427–1448, https://doi.org/10.1093/petrology/egn031.

Camejo-Harry, M., Melekhova, E., Blundy, J., Attridge, W., Robertson, R. and Christopher, T. 2018. Magma evolution beneath Bequia, Lesser Antilles, deduced from petrology of lavas and plutonic xenoliths. *Contributions to Mineralogy and Petrology*, **173**, 77, https://doi.org/10.1007/s00410-018-1504-z.

Caricchi, L., Annen, C., Blundy, J., Simpson, G. and Pinel, V. 2014. Frequency and magnitude of volcanic eruptions controlled by magma injection and buoyancy. *Nature Geoscience*, **7**, 126–130, https://doi.org/10.1038/ngeo2041.

Caricchi, L., Sheldrake, T.E. and Blundy, J. 2018. Modulation of magmatic processes by CO2 flushing. *Earth and Planetary Science Letters*, **491**, 160–171, https://doi.org/10.1016/j.epsl.2018.03.042.

Cashman, K.V. 1992. Groundmass crystallization of Mount St. Helens dacite, 1980–1986: a tool for interpreting shallow magmatic processes. *Contributions to Mineralogy and Petrology*, **109**, 431–449, https://doi.org/10.1007/BF00306547.

Cashman, K.V. and Marsh, B.D. 1988. Crystal size distribution (CSD) in rocks and the kinetics and dynamics of crystallization II: Makaopuhi lava lake. *Contributions to Mineralogy and Petrology*, **99**, 292–305, https://doi.org/10.1007/BF00375363.

Cashman, K.V. and McConnell, S.M. 2005. Multiple levels of magma storage during the 1980 summer eruptions of Mount St. Helens, WA. *Bulletin of Volcanology*, **68**, 57–75, https://doi.org/10.1007/s00445-005-0422-x.

Cassidy, M., Manga, M., Cashman, K. and Bachmann, O. 2018. Controls on explosive-effusive volcanic eruption styles. *Nature Communications*, **9**, 2839, https://doi.org/10.1038/s41467-018-05293-3.

Castro, J.M. and Gardner, J.E. 2008. Did magma ascent rate control the explosive-effusive transition at the Inyo volcanic chain, California. *Geology*, **36**, 279, https://doi.org/10.1130/G24453A.1.

Castro, J.M., Cashman, K.V. and Manga, M. 2003. A technique for measuring 3D crystal-size distributions of prismatic microlites in obsidian. *American Mineralogist*, **88**, 1230–1240, https://doi.org/10.2138/am-2003-8-906.

Cole, P.D., Robertson, R.E.A., Fedele, L. and Scarpati, C. 2019. Explosive activity of the last 1000 years at La Soufrière, St Vincent, Lesser Antilles. *Journal of Volcanology and Geothermal Research*, **371**, 86–100, https://doi.org/10.1016/j.jvolgeores.2019.01.002.

Corsaro, R.A. and Miraglia, L. 2022. Near Real-Time Petrologic Monitoring on Volcanic Glass to Infer Magmatic Processes During the February–April 2021 Paroxysms of the South-East Crater, Etna. *Frontiers in Earth Science*, **10**.

Devine, J.D., Rutherford, M.J., Norton, G.E. and Young, S.R. 2003. Magma Storage Region Processes Inferred from Geochemistry of Fe–Ti Oxides in Andesitic Magma, Soufrière Hills Volcano, Montserrat, W.I. *Journal of Petrology*, **44**, 1375–1400, https://doi.org/10.1093/petrology/44.8.1375.

Druitt, T.H., Costa, F., Deloule, E., Dungan, M. and Scaillet, B. 2012. Decadal to monthly timescales of magma transfer and reservoir growth at a caldera volcano. *Nature*, **482**, 77–80, https://doi.org/10.1038/nature10706.

Dualeh, E.W., Ebmeier, S.K., et al. 2023. Rapid pre-explosion increase in dome extrusion rate at La Soufrière, St. Vincent quantified from synthetic aperture radar backscatter. *Earth and Planetary Science Letters*, **603**, 117980, https://doi.org/10.1016/j.epsl.2022.117980.

Edmonds, M., Kohn, S.C., Hauri, E.H., Humphreys, M.C.S. and Cassidy, M. 2016. Extensive, water-rich magma reservoir beneath southern Montserrat. *Lithos*, **252–253**, 216–233, https://doi.org/10.1016/j.lithos.2016.02.026.

Eichelberger, J.C. and Izbekov, P.E. 2000. Eruption of andesite triggered by dyke injection: contrasting cases at Karymsky Volcano, Kamchatka and Mt Katmai, Alaska.

Philosophical Transactions of the Royal Society of London. Series A: Mathematical, Physical and Engineering Sciences, https://doi.org/10.1098/rsta.2000.0599.

Fedele, L., Cole, P.D., Scarpati, C. and Robertson, R.E.A. 2021. Petrological insights on the last 1000 years of explosive activity at La Soufrière volcano, St. Vincent (Lesser Antilles). *Lithos*, **392–393**, 106150, https://doi.org/10.1016/j.lithos.2021.106150.

Frey, H.M. and Lange, R.A. 2011. Phenocryst complexity in andesites and dacites from the Tequila volcanic field, Mexico: resolving the effects of degassing vs. magma mixing. *Contributions to Mineralogy and Petrology*, **162**, 415–445, https://doi.org/10.1007/s00410-010-0604-1.

Frey, H.M., Manon, M.R.F., Brehm, S.K. and Babiak, R.N. 2018. Episodic crystallization in young explosive eruptions in Dominica, Lesser Antilles, revealed by U-Th dating of zircons. *Geology*, **46**, 887–890, https://doi.org/10.1130/G45217.1.

Frost, B.R. and Lindsley, D.H. 1991. Occurrence of iron-titanium oxides in igneous rocks. *Reviews in Mineralogy and Geochemistry*, **25**, 433–468.

Gonnermann, H.M. and Manga, M. 2007. The Fluid Mechanics Inside a Volcano. *Annual Review of Fluid Mechanics*, **39**, 321–356, https://doi.org/10.1146/annurev.fluid.39.050905.110207.

Graham, A.M. and Thirlwall, M.F. 1981. Petrology of the 1979 eruption of Soufriere volcano, St. Vincent, Lesser Antilles. *Contributions to Mineralogy and Petrology*, **76**, 336–342, https://doi.org/10.1007/BF00375460.

Grove, T.L. and Juster, T.C. 1989. Experimental investigations of low-Ca pyroxene stability and olivine-pyroxene-liquid equilibria at 1-atm in natural basaltic and andesitic liquids. *Contributions to Mineralogy and Petrology*, **103**, 287–305, https://doi.org/10.1007/BF00402916.

Hammer, J.E., Cashman, K.V., Hoblitt, R.P. and Newman, S. 1999. Degassing and microlite crystallization during pre-climactic events of the 1991 eruption of Mt. Pinatubo, Philippines. *Bulletin of Volcanology*, **60**, 355–380, https://doi.org/10.1007/s004450050238.

Heath, E., Macdonald, R., Belkin, H., Hawkesworth, C. and Sigurdsson, H. 1998. Magmagenesis at Soufriere Volcano, St Vincent, Lesser Antilles Arc. **39**, 44.

Higgins, M.D. 2000. Measurement of crystal size distributions. *American Mineralogist*, **85**, 1105–1116, https://doi.org/10.2138/am-2000-8-901.

Housh, T. and Luhr, J.F. 1991. Plagioclase-melt equilibria in hydrous systems. *American Mineralogist*, **76**, 477–492.

Humphreys, M.C.S., Blundy, J.D. and Sparks, R.S.J. 2006. Magma Evolution and Open-System Processes at Shiveluch Volcano: Insights from Phenocryst Zoning. *Journal of Petrology*, **47**, 2303–2334, https://doi.org/10.1093/petrology/egl045.

Humphreys, M.C.S., Christopher, T. and Hards, V. 2009. Microlite transfer by disaggregation of mafic inclusions following magma mixing at Soufrière Hills volcano, Montserrat.

Contributions to Mineralogy and Petrology, **157**, 609–624, https://doi.org/10.1007/s00410-008-0356-3.

Humphreys, M.C.S., Edmonds, M. and Klöcking, M.S. 2016. The validity of plagioclase-melt geothermometry for degassing-driven magma crystallization. *American Mineralogist*, **101**, 769–779, https://doi.org/10.2138/am-2016-5314.

Joseph, E.P., Camejo-Harry, M., et al. 2022. Responding to eruptive transitions during the 2020–2021 eruption of La Soufrière volcano, St. Vincent. *Nature Communications*, **13**, 4129, https://doi.org/10.1038/s41467-022-31901-4.

Kent, A.J.R., Blundy, J., et al. 2007. Vapor transfer prior to the October 2004 eruption of Mount St. Helens, Washington. *Geology*, **35**, 231, https://doi.org/10.1130/G22809A.1.

Kent, A.J.R., Darr, C., Koleszar, A.M., Salisbury, M.J. and Cooper, K.M. 2010. Preferential eruption of andesitic magmas through recharge filtering. *Nature Geoscience*, **3**, 631–636, https://doi.org/10.1038/ngeo924.

Kress, V.C. and Carmichael, I.S.E. 1991. The compressibility of silicate liquids containing Fe2O3 and the effect of composition, temperature, oxygen fugacity and pressure on their redox states. *Contributions to Mineralogy and Petrology*, **108**, 82–92, https://doi.org/10.1007/BF00307328.

Lange, R.A., Frey, H.M. and Hector, J. 2009. A thermodynamic model for the plagioclase-liquid hygrometer/thermometer. *American Mineralogist*, **94**, 494–506, https://doi.org/10.2138/am.2009.3011.

Lindoo, A., Larsen, J.F., Cashman, K.V. and Oppenheimer, J. 2017. Crystal controls on permeability development and degassing in basaltic andesite magma. *Geology*, **45**, 831–834, https://doi.org/10.1130/G39157.1.

Lormand, C., Zellmer, G.F., et al. 2020. Shallow magmatic processes revealed by cryptic microantecrysts: a case study from the Taupo Volcanic Zone. *Contributions to Mineralogy and Petrology*, **176**, 97, https://doi.org/10.1007/s00410-021-01857-7.

Lormand, C., Zellmer, G.F., et al. 2021. Slow Ascent of Unusually Hot Intermediate Magmas Triggering Strombolian to Sub-Plinian Eruptions. *Journal of Petrology*, **61**, egaa077, https://doi.org/10.1093/petrology/egaa077.

Malfait, W.J., Seifert, R., et al. 2014. Supervolcano eruptions driven by melt buoyancy in large silicic magma chambers. *Nature Geoscience*, **7**, 122–125, https://doi.org/10.1038/ngeo2042.

Mangler, M.F., Humphreys, M.C.S., Wadsworth, F.B., Iveson, A.A. and Higgins, M.D. 2022. Variation of plagioclase shape with size in intermediate magmas: a window into incipient plagioclase crystallisation. *Contributions to Mineralogy and Petrology*, **177**, 64, https://doi.org/10.1007/s00410-022-01922-9.

Martel, C. 2012. Eruption Dynamics Inferred from Microlite Crystallization Experiments: Application to Plinian and Dome-forming Eruptions of Mt. Pelée (Martinique, Lesser

Antilles). *Journal of Petrology*, **53**, 699–725, https://doi.org/10.1093/petrology/egr076.

Martel, C., Pichavant, M., Holtz, F., Scaillet, B., Bourdier, J.-L. and Traineau, H. 1999. Effects of f O2 and H2O on andesite phase relations between 2 and 4 kbar. *Journal of Geophysical Research: Solid Earth*, **104**, 29453–29470, https://doi.org/10.1029/1999JB900191.

Martel, C., Radadi Ali, A., Poussineau, S., Gourgaud, A. and Pichavant, M. 2006. Basalt-inherited microlites in silicic magmas: Evidence from Mount Pelée (Martinique, French West Indies). *Geology*, **34**, 905–908, https://doi.org/10.1130/G22672A.1.

Melekhova, E., Blundy, J., Robertson, R. and Humphreys, M.C.S. 2015. Experimental Evidence for Polybaric Differentiation of Primitive Arc Basalt beneath St. Vincent, Lesser Antilles. *Journal of Petrology*, **56**, 161–192, https://doi.org/10.1093/petrology/egu074.

Moitra, P., Gonnermann, H.M., Houghton, B.F. and Tiwary, C.S. 2018. Fragmentation and Plinian eruption of crystallizing basaltic magma. *Earth and Planetary Science Letters*, **500**, 97–104, https://doi.org/10.1016/j.epsl.2018.08.003.

Mollo, S., Putirka, K., Iezzi, G., Del Gaudio, P. and Scarlato, P. 2011. Plagioclase–melt (dis)equilibrium due to cooling dynamics: Implications for thermometry, barometry and hygrometry. *Lithos*, **125**, 221–235, https://doi.org/10.1016/j.lithos.2011.02.008.

Mollo, S., Putirka, K., Iezzi, G. and Scarlato, P. 2013. The control of cooling rate on titanomagnetite composition: implications for a geospeedometry model applicable to alkaline rocks from Mt. Etna volcano. *Contributions to Mineralogy and Petrology*, **165**, 457–475, https://doi.org/10.1007/s00410-012-0817-6.

Moore, G. and Carmichael, I.S.E. 1998. The hydrous phase equilibria (to 3 kbar) of an andesite and basaltic andesite from western Mexico: constraints on water content and conditions of phenocryst growth. *Contributions to Mineralogy and Petrology*, **130**, 304–319, https://doi.org/10.1007/s004100050367.

Mujin, M. and Nakamura, M. 2014. A nanolite record of eruption style transition. *Geology*, **42**, 611–614, https://doi.org/10.1130/G35553.1.

Mujin, M., Nakamura, M. and Miyake, A. 2017. Eruption style and crystal size distributions: Crystallization of groundmass nanolites in the 2011 Shinmoedake eruption. *American Mineralogist*, **102**, 2367–2380, https://doi.org/10.2138/am-2017-6052CCBYNCND.

Murch, A.P. and Cole, P.D. 2019. Using microlites to gain insights into ascent conditions of differing styles of volcanism at Soufrière Hills Volcano. *Journal of Volcanology and Geothermal Research*, **384**, 221–231, https://doi.org/10.1016/j.jvolgeores.2019.07.022.

Panjasawatwong, Y., Danyushevsky, L.V., Crawford, A.J. and Harris, K.L. 1995. An experimental study of the effects of melt composition on plagioclase-melt equilibria at 5 and 10 kbar: implications for the origin of magmatic high-An plagioclase. *Contributions to Mineralogy and Petrology*, **118**, 420–432, https://doi.org/10.1007/s004100050024.

Pankhurst, M.J., Scarrow, J.H., et al. 2022. Rapid response petrology for the opening eruptive phase of the 2021 Cumbre Vieja eruption, La Palma, Canary Islands. *Volcanica*, **5**, 1–10, https://doi.org/10.30909/vol.05.01.0110.

Petrelli, M., El Omari, K., Spina, L., Le Guer, Y., La Spina, G. and Perugini, D. 2018. Timescales of water accumulation in magmas and implications for short warning times of explosive eruptions. *Nature Communications*, **9**, 770, https://doi.org/10.1038/s41467-018-02987-6.

Pichavant, M. and Macdonald, R. 2007. Crystallization of primitive basaltic magmas at crustal pressures and genesis of the calc-alkaline igneous suite: experimental evidence from St Vincent, Lesser Antilles arc. *Contributions to Mineralogy and Petrology*, **154**, 535–558, https://doi.org/10.1007/s00410-007-0208-6.

Pichavant, M., Mysen, B.O. and Macdonald, R. 2002a. Source and H2O content of high-MgO magmas in island arc settings: an experimental study of a primitive calc-alkaline basalt from St. Vincent, Lesser Antilles arc. *Geochimica et Cosmochimica Acta*, **66**, 2193–2209, https://doi.org/10.1016/S0016-7037(01)00891-2.

Pichavant, M., Mysen, B.O. and Macdonald, R. 2002b. Source and H2O content of high-MgO magmas in island arc settings: an experimental study of a primitive calc-alkaline basalt from St. Vincent, lesser antilles arc. *Geochimica et Cosmochimica Acta*, **66**, 2193–2209, https://doi.org/10.1016/S0016-7037(01)00891-2.

Popa, R.-G., Bachmann, O. and Huber, C. 2021. Explosive or effusive style of volcanic eruption determined by magma storage conditions. *Nature Geoscience*, **14**, 781–786, https://doi.org/10.1038/s41561-021-00827-9.

Preece, K., Barclay, J., Gertisser, R. and Herd, R.A. 2013. Textural and micro-petrological variations in the eruptive products of the 2006 dome-forming eruption of Merapi volcano, Indonesia: Implications for sub-surface processes. *Journal of Volcanology and Geothermal Research*, **261**, 98–120, https://doi.org/10.1016/j.jvolgeores.2013.02.006.

Rasmussen, D.J., Plank, T.A., Roman, D.C. and Zimmer, M.M. 2022. Magmatic water content controls the pre-eruptive depth of arc magmas. *Science*, **375**, 1169–1172, https://doi.org/10.1126/science.abm5174.

Re, G., Corsaro, R.A., D'Oriano, C. and Pompilio, M. 2021. Petrological monitoring of active volcanoes: A review of existing procedures to achieve best practices and operative protocols during eruptions. *Journal of Volcanology and Geothermal Research*, **419**, 107365, https://doi.org/10.1016/j.jvolgeores.2021.107365.

Robertson, R. 1995. An assessment of the risk from future eruptions of the Soufriere volcano of St. Vincent, West Indies. *Natural Hazards*, **11**, 163–191, https://doi.org/10.1007/BF00634531.

Roeder, P.L. and Emslie, R.F. 1970. Olivine-liquid equilibrium. *Contributions to Mineralogy and Petrology*, **29**, 275–289, https://doi.org/10.1007/BF00371276.

Ruprecht, P. and Wörner, G. 2007. Variable regimes in magma systems documented in plagioclase zoning patterns: El Misti stratovolcano and Andahua monogenetic cones.

Journal of Volcanology and Geothermal Research, **165**, 142–162, https://doi.org/10.1016/j.jvolgeores.2007.06.002.

Shea, T. and Hammer, J.E. 2013. Kinetics of cooling- and decompression-induced crystallization in hydrous mafic-intermediate magmas. *Journal of Volcanology and Geothermal Research*, **260**, 127–145, https://doi.org/10.1016/j.jvolgeores.2013.04.018.

Sisson, T.W. and Grove, T.L. 1993. Experimental investigations of the role of H2O in calc-alkaline differentiation and subduction zone magmatism. *Contributions to Mineralogy and Petrology*, **113**, 143–166, https://doi.org/10.1007/BF00283225.

Sparks, S.R.J., Sigurdsson, H. and Wilson, L. 1977. Magma mixing: a mechanism for triggering acid explosive eruptions. *Nature*, **267**, 315–318, https://doi.org/10.1038/267315a0.

Stamper, C.C., Blundy, J.D., Arculus, R.J. and Melekhova, E. 2014. Petrology of Plutonic Xenoliths and Volcanic Rocks from Grenada, Lesser Antilles. *Journal of Petrology*, **55**, 1353–1387, https://doi.org/10.1093/petrology/egu027.

Stock, M.J., Humphreys, M.C.S., Smith, V.C., Isaia, R. and Pyle, D.M. 2016. Late-stage volatile saturation as a potential trigger for explosive volcanic eruptions. *Nature Geoscience*, **9**, 249–254, https://doi.org/10.1038/ngeo2639.

Tollan, P.M.E., Bindeman, I. and Blundy, J.D. 2012. Cumulate xenoliths from St. Vincent, Lesser Antilles Island Arc: a window into upper crustal differentiation of mantle-derived basalts. *Contributions to Mineralogy and Petrology*, **163**, 189–208, https://doi.org/10.1007/s00410-011-0665-9.

Toramaru, A., Noguchi, S., Oyoshihara, S. and Tsune, A. 2008. MND(microlite number density) water exsolution rate meter. *Journal of Volcanology and Geothermal Research*, **175**, 156–167, https://doi.org/10.1016/j.jvolgeores.2008.03.035.

Utami, S.B., Costa, F., Lesage, P., Allard, P. and Humaida, H. 2021. Fluid Fluxing and Accumulation Drive Decadal and Short-Lived Explosive Basaltic Andesite Eruptions Preceded by Limited Volcanic Unrest. *Journal of Petrology*, **62**, egab086, https://doi.org/10.1093/petrology/egab086.

Utami, S.B., Andùjar, J., Costa, F., Scaillet, B., Humaida, H. and Carn, S. 2022. Pre-eruptive excess volatiles and their relationship to effusive and explosive eruption styles in semi-plugged volcanoes. *Frontiers in Earth Science*, **10**.

Waters, L.E. and Lange, R.A. 2015. An updated calibration of the plagioclase-liquid hygrometer-thermometer applicable to basalts through rhyolites. *American Mineralogist*, **100**, 2172–2184, https://doi.org/10.2138/am-2015-5232.

Waters, L.E., Andrews, B.J. and Frey, H.M. 2021. Daly Gaps at South Sister, Oregon, USA, generated via partial melting. *Contributions to Mineralogy and Petrology*, **176**, 52, https://doi.org/10.1007/s00410-021-01805-5.

Zellmer, G.F., Pistone, M., Iizuka, Y., Andrews, B.J., Gómez-Tuena, A., Straub, S.M. and Cottrell, E. 2016. Petrogenesis of antecryst-bearing arc basalts from the Trans-

Mexican Volcanic Belt: Insights into along-arc variations in magma-mush ponding depths, H2O contents, and surface heat flux. *American Mineralogist*, **101**, 2405–2422, https://doi.org/10.2138/am-2016-5701.

Camejo-Harry, M., Pascal K., Ryan, G. This volume. Pre and Syn deformation associated with the La Soufriere volcanic eruption of 2020-21.

Christopher, T.E., Frey, H.M., Mourne, S. Manon, M.R., Contreras, R., Barclay, J., Davies, B.V., Cole, P.D., Joseph, E.P., Robertson, R., Henry L., and Howe, T. This volume. Insights into the dynamics of the (2020-2021) La Soufriere eruption revealed from vesicle size distribution and degassing studies.

Cole, P.D., Barclay, J., Robertson, R.E.A., Mitchell, S., Davies, B.V., Constantanescu, R., Sparks R.S.J., Aspinall, W. and Stinton A. This volume. Explosive sequence of La Soufrière St Vincent April 2021: insights into drivers and consequences via eruptive products.

Morrison-Evans, B., Melekhova, E., Blundy, J. This volume. Experimental insight into basaltic andesite lava dome oxidation textures at La Soufrière, St Vincent.

Sparks, R.S.J., Aspinall, W., Barclay, J., Renfrew, I. and Stewart, R. This volume. Analysis of magma flux and eruption intensity during the explosive activity at Soufrière St Vincent.

Stinton, A., Sparks, R.S.J. and Huppert, H. E. This volume. Analysis of magma rheology from lava spreading and explosive activity during the 2020-2021 eruption of the Soufrière St Vincent with implications for eruption dynamics.

Weber, G. Blundy, J., Barclay, J., Pyle, D.M., Cole, P.D., Frey, H.M., Manon, M.R., Davies, B.V., and Cashman, K.V. This volume. Petrology of the 2020-21 effusive to explosive eruption of La Soufrière volcano, St Vincent: Insights into plumbing system architecture and magma assembly mechanism.

Figure Captions

Fig. 1. Location map of La Soufrière, St Vincent. a) St. Vincent is in the southern segment of the Lesser Antilles arc. b) La Soufrière is located in the northern third of the island. The central vent/lava dome is visible and tephra sample locations are shown in yellow circles. Scoria analyzed in this study include distal deposits from Rabacca and Sandy Bay and proximal deposits from Jacobs Well, marked in pink.

Fig. 2. Representative field image of a proximal tephra deposit from the 2021 La Soufrière eruption, with units and stratigraphy as defined by Cole *et al.* (this volume).

Fig. 3. Elemental map of a vesicular scoria clast from U5 produced by wavelength dispersive spectrometry (WDS). The individual element color maps have been optimized to allow for differentiation of the various phenocryst phases and coarse zoning patterns. Orange – plagioclase; green – olivine; pink – clinopyroxene; teal – orthopyroxene; blue – titanomagnetite. Scale bar is 1.5 mm.

Fig. 4. Backscattered electron (BSE) images of 2021 scoria clasts in U5. These images show representative phenocrysts, macro features, and textures. a) typical phenocryst and microlite phase assemblage in a vesicular groundmass; the crystals lack complex zoning or disequilibrium textures. b) plagioclase phenocrysts display normal zoning. Note the abrupt transition between core and rim and thickness of the rim. c) euhedral olivine crystals. d) orthopyroxene, clinopyroxene, and titanomagnetite phenocrysts. e) glomerocryst comprised of multiple phases. f) rare glomerocryst with abundant alteration and breakdown textures. Textures are similar to samples from the 2021 lava dome and the glomerocryst is interpreted as a rock fragment of the dome entrained in the explosive eruption. Major phases are annotated as: plag: plagioclase, pyx: pyroxene, cpx: clinopyroxene, opx: orthopyroxene, ox: Fe-Ti oxide, ol: olivine, ap: apatite, py: pyrite. An is anorthite content in plagioclase and Fo is forsterite content in olivine. Scale bars are 200 μm.

Fig. 5. Stacked histograms of plagioclase phenocryst anorthite (An) content show a broad compositional range that is comparable throughout the effusive and explosive eruptions. Data for the dome and some U5 samples from are from Weber *et al.* (this volume).

Fig. 6. Compositional comparison between phenocrysts and microlites in the lava dome and scoria. U1 microlites are highlighted by orange squares, as they have compositions which differ from the other explosive phases. a) Variation of plagioclase anorthite content with FeO_{total}. b) Variation of olivine forsterite content with CaO. c) Variation of pyroxene compositions with respect to quadrilateral components. Dashed line shows the pyroxene solvus at 1000˚C and 1200 ˚C from Lindsley & Anderson (1983). d) Variation of TiO_2 with MnO for titanomagnetite.

Fig. 7. Composition of the residual glass in the scoria from each explosive phase of the eruption based on a 5 μm defocused beam analysis. The U5 groundmass analysis is from a 20 μm defocused beam analysis of glass and microlites by Weber *et al.* (this volume). Each analysis is shown as a black circle, with mean and quartiles denoted by the vertical lines and colored regions.

Fig. 8. Backscattered electron (BSE) images of microlites in the effusive and explosive phases of the 2021 eruption highlighting the textural and phase abundance differences. a) Dome microlites are dominated by An-poor unzoned plagioclase, acicular orthopyroxene and titanomagnetite. Some opx are rimmed by small oxide microlites. b) U1 is characterized by small vesicles, abundant microlite crystallization, normally zoned plagioclase and olivine. c-e) U2-U5 are characterized by larger

vesicles, lower microlite crystallinity, zoned and unzoned plagioclase and a variety of pyroxenes and titanomagnetite. f) EDS Elemental map of U5 sample. The smallest microlite populations consist of albitic plagioclase (pale red) and intermediate pyroxene (light pink), with minor magnetite (blue) and no olivine (yellow). White scale bar is 50 μm in all images.

Fig. 9. Crystal size distributions (CSD) for combined lava dome (dashed line), U1, U2 and U5 scoria clasts. Black line at long axis 30 μm marks boundary between microlites and microphenocrysts. Grey line at ~20 μm marks length below which crystals from U1 will have widths too small (<5 μm) for EMPA analysis. Inset is Zingg plot of best-fit 3D crystal aspect ratios calculated for full datasets using ShapeCalc (Mangler *et al.* 2022).

Fig. 10. Length of plagioclase microphenocrysts and microlites with respect to anorthite content of crystal cores (closed symbols) and crystal rims (open symbols). The larger crystals tend to be zoned and have more calcic cores than the unzoned plagioclase. The zoned cores span a broad compositional range (An_{43-96}), whereas the unzoned crystals have a more restricted An-poor composition ($<An_{70}$). The rims of the zoned crystals of all sizes have a similar composition to the unzoned plagioclase.

Fig. 11. Stacked histograms of plagioclase microlite compositions with respect to anorthite and olivine microlite compositions with respect to forsterite. a) Dome microlites are the most sodic, with most crystals An_{40-55}. U1 has a bimodal population, with a significant number of zoned crystals with $>An_{70}$ and a second lower-An population comprised of unzoned crystals and rims of zoned crystals. U2-U5 show a similar pattern, with fewer zoned plagioclase microlites and more lower-An unzoned crystals. b) Note that the dome eruption is not plotted, as olivine was not present as a microlite. All olivine analyses are cores. U1 has abundant olivine microlites with Fo_{62-80}. U2-U5 have very few olivine microlites, but a similar range in composition compared to U1.

Fig. 12. Comparison of pyroxene microlites in each eruptive unit with respect to CaO and Al_2O_3.

Fig. 13. An assessment of microlite compositions with respect to the proposed carrier melt in comparison to hydrous and anhydrous phase equilibrium experiments, as compiled by Waters et al. (2021) and discussed in the text. The liquid An-number is defined as the ratio of the anorthite component in the liquid divided by the sum of the anorthite and albite components in the liquid, where $X_{An}^{liq} = 64.0(X_{CaO})(X_{Al2O3})(X_{SiO2})^2$ and $X_{Ab}^{liq} = 18.963(X_{Na2O})(X_{AlO3})^{0.5}(X_{SiO2})^3$. a) Plagioclase microlite high-An cores do not overlap with the experimental dataset, whereas unzoned microlites and rims are similar to compositions found in hydrous experiments. b) Part of the lower-Mg# compositional range of the opx microlites overlaps with the experimental data. c) Part of the lower-Mg# compositional range of the cpx microlites overlaps with the experimental data.

Fig. 14. Conceptual model of the effusive and multiple explosive events during the 2020-21 eruption of La Soufrière St Vincent. The eruptive products, as categorized by microlite assemblages and compositions, are derived from three different batches of magma. During ascent, magmas crystallized microlites and scavenged glomerocrysts and xenocrysts, leading to a complex crystal cargo. a) The effusive phase of the eruption was characterized by an altered crystalline groundmass dominated by low-An plagioclase, orthopyroxene, and titanomagnetite (batch 1 melt) that is distinctive from the scoria microlite assemblages. b) During late March, An-rich plagioclase and Fo-poor olivine microlites begin to crystallize from a water-rich mafic melt at depth (batch 2) and stalls, leading to fluid saturation. c) By early April, this crystallization has induced second boiling and fluids and melt begin to ascend, leading to nucleation of a juvenile population of microlites and eruption on April 9th. The eruption has microlites that formed at depth, as well as during ascent (e.g. zoned plagioclase) d)

Following the catastrophic eruption and deflation, more magma ascends (batch 3), crystallizing microlites and incorporating remnants of batch 2 during eruption phases U2 and U3. e) On April 11th, the largest explosions (U5) occur, driven by the unencumbered ascent of melt batch 3, now featuring larger bubbles and a lower crystallinity, with little evidence of batch 2 melts, which were characterized by the distinctive olivine and high-An microlites observed in U1.

Table Captions

Table 1. Representative microprobe analyses of microlites

Table 2. Textural variation and microlite crystallinity of the 2020-21 La Soufriere eruption

Table 3. Relative proportion of mafic microlites from phase counts on BSE images and EDS spectra

	Plagioclase	Plagioclase	Plagioclase	Plagioclase		Pyroxene	Pyroxene	Pyroxene	Pyroxene		Olivine	Olivine	Olivine	Olivine		Magnetite	Magnetite	Magnetite	Magnetite	
	U1	U1	U1	U1		U1	U1	U5	U5		U1	U1	U2	U2		Dome	U1	U1	U2	
	Core	Rim				Cpx	Opx	Int. Px	Int. Px											
SiO2	48.78	52.65	44.42	53.91		48.89	53.53	51.49	51.64		38.92	38.28	36.82	38.13		0.20	0.11	0.15	0.19	
TiO2	0.04	0.04	0.02	0.06		0.86	0.19	0.74	0.58							11.01	12.71	12.30	14.70	
Al2O3	31.49	28.99	34.97	28.80		5.81	0.62	2.99	2.43		0.02	0.02	0.08	0.03		1.35	3.38	3.34	2.60	
Cr2O3						0.00	0.00	0.00	0.00		0.00	0.00	0.02	0.00		0.03	0.08	0.09	0.08	
V2O3																0.25	0.80	0.74	0.68	
Fe2O3																46.39	43.22	43.32	37.74	
NiO						0.00	0.00	0.00	0.00		0.04	0.02	0.08	0.04		0.00	0.00	0.00	0.00	
MgO	0.10	0.08	0.05	0.10		14.15	23.76	16.13	18.92		40.29	37.70	29.19	37.39		2.31	3.08	2.88	2.04	
FeO	0.85	0.77	0.68	0.85		8.39	19.66	14.15	15.79		19.72	23.34	32.69	22.69		35.97	34.85	34.50	38.61	
MnO						0.19	0.64	0.62	0.69		0.35	0.39	0.74	0.38		0.91	0.46	0.48	0.56	
CaO	15.46	12.51	18.93	11.50		20.80	1.54	14.39	9.81		0.21	0.22	0.24	0.19						
Na2O	2.75	4.28	0.80	4.86		0.25	0.13	0.27	0.19											
K2O	0.04	0.08	0.02	0.08		0.00	0.00	0.00	0.00											
total	99.51	99.39	99.90	100.15		99.34	100.08	100.78	100.04		99.55	99.96	99.89	98.84		93.87	94.64	93.78	93.60	
																98.52	98.97	98.12	97.38	*recalc. tot.*
formula calc.	8	8	0	0		6	6	6	6		4	4	4	4		3	3	3	3	
Si	2.251	2.407	2.061	2.440		1.820	1.970	1.909	1.916		1.004	1.002	1.011	1.006		0.0074	0.0039	0.0055	0.0071	
Ti	0.001	0.001	0.001	0.002		0.024	0.005	0.021	0.016							0.3120	0.3522	0.3439	0.4183	
Al	1.712	1.562	1.913	1.536		0.255	0.027	0.131	0.106		0.001	0.001	0.003	0.001		0.0598	0.1469	0.1464	0.1156	
Cr											0.000	0.000	0.001	0.000		0.0009	0.0023	0.0026	0.0022	
V																0.0075	0.0235	0.0222	0.0206	
Ni											0.001	0.000	0.002	0.001						
Mg	0.007	0.006	0.003	0.006		0.786	1.303	0.891	1.047		1.550	1.470	1.195	1.471		0.1299	0.1692	0.1596	0.1149	
Fe3+	0.033	0.029	0.026	0.032		0.074	0.033	0.030	0.043							1.3156	1.1978	1.2119	1.0739	
Fe2+						0.188	0.572	0.409	0.447		0.426	0.511	0.751	0.501		1.1335	1.0735	1.0728	1.2209	
Mn	0.000	0.000	0.000	0.000		0.006	0.020	0.019	0.022		0.008	0.009	0.017	0.008		0.0289	0.0144	0.0151	0.0180	
Ca	0.764	0.613	0.941	0.558		0.830	0.061	0.572	0.390		0.006	0.006	0.007	0.005		0.0046	0.0040	0.0047	0.0072	
Na	0.246	0.380	0.072	0.427		0.018	0.009	0.019	0.013											
K	0.002	0.004	0.001	0.005		0.000	0.000	0.000	0.000											
cation tot.	5.016	5.003	0.000	0.000		4	4	4	4		2.995	2.998	2.987	2.993		4	4	4	4	
mol %	75.5	61.5	92.7	56.4	*An*	43.6	67.3	47.6	55.6	*En*	78.5	74.2	61.4	74.6	*Fo*	11.3	13.4	13.1	15.4	*Rt*
mol %	24.3	38.1	7.1	43.1	*Ab*	10.4	29.5	21.8	23.7	*Fs*	21.5	25.8	38.6	25.4	*Fa*	41.1	40.9	40.8	45.0	*Ulv*
mol %	0.2	0.4	0.1	0.5	*Or*	46.0	3.1	30.5	20.7	*Wo*						47.6	45.7	46.1	39.6	*Hem*

Table 1

Eruption Phase	Sample	Crytals Analyzed (n)	Analysed Area[a] (mm^2)	Feldspar[a] (%)	Mafics[a,b] (%)	Oxide[a] (%)	Vesicles[a] (%)	Glass[a] (%)	Microlite Crystallinity (Feldspar)	Aspect Ratio[c]	Mean Crystal Area (µm ^{2})	Median Crystal Area (µm ^{2})
Dome	SVG21-16-2&5	3160	0.20000	38.01	12.08	5.39	8.66	35.86	0.32	1 : 2.7 : 5.6	16.14	5.44
U1 Scoria	LS21-72	1830	0.04826	15.82	6.45	0.24	39.39	38.13	0.29	1 : 4.3 : 6.4	4.18	1.97
U2 Scoria	LS21-98 sc	729	0.07746	8.99	4.46	0.94	51.02	34.59	0.21	1 : 3.5 : 5.2	9.54	4.61
U5 Scoria	LS21-34	655	0.12692	13.76	2.32	0.86	35.11	47.95	0.22	1 : 2.2 : 6.4	24.4	9.69

[a]*Abundance corrected for area analyses minus partial crystals*

[b]*mafics include undifferentiated olivine and pyroxene*

[c]*calculated from ShapeCalc*

Table 2

Eruptive Unit	Ol (%)	Opx (%)	Cpx (%)	Int. Px (%)	Ox (%)	n, mafics
Dome	0	58	4	7	31	180
U1 Scoria	44	7	13	1	35	491
U2 Scoria	19	18	15	12	36	383
U3 Scoria	14	7	18	22	38	170
U5 Scoria	12	30	21	6	31	247

Table 3

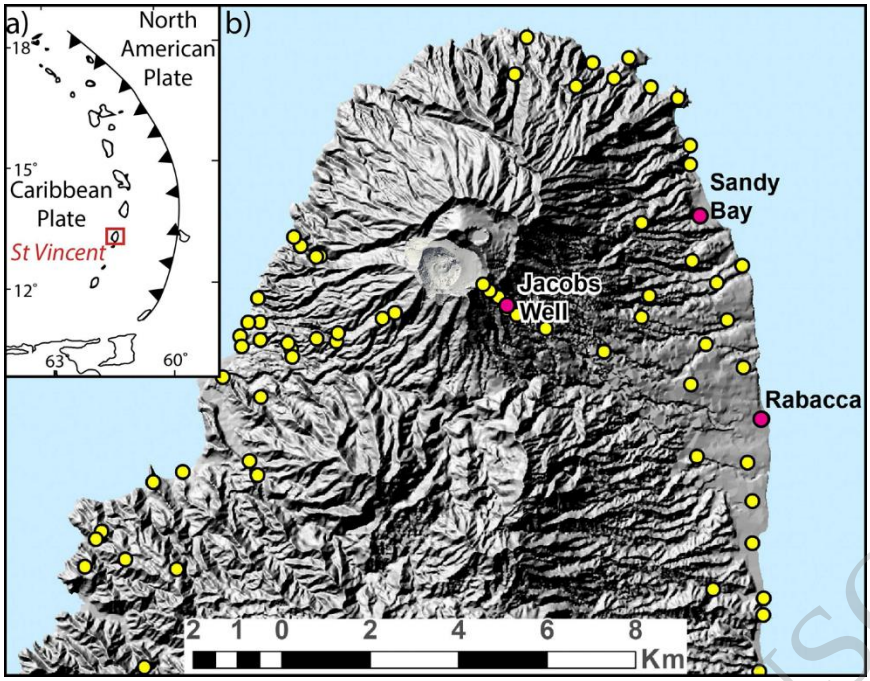

Figure 1

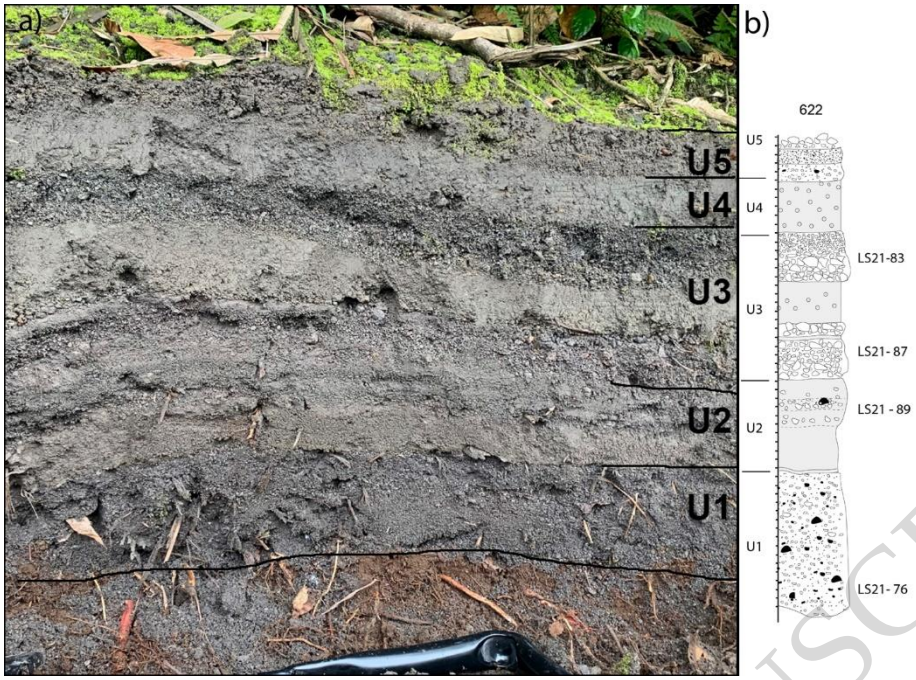

Figure 2

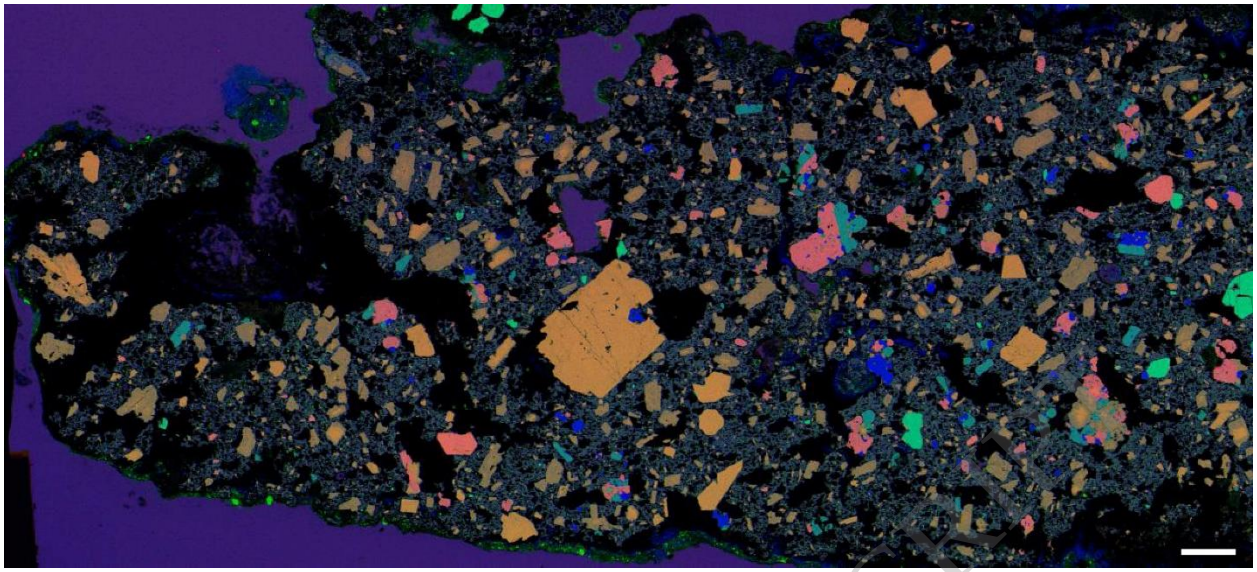

Figure 3

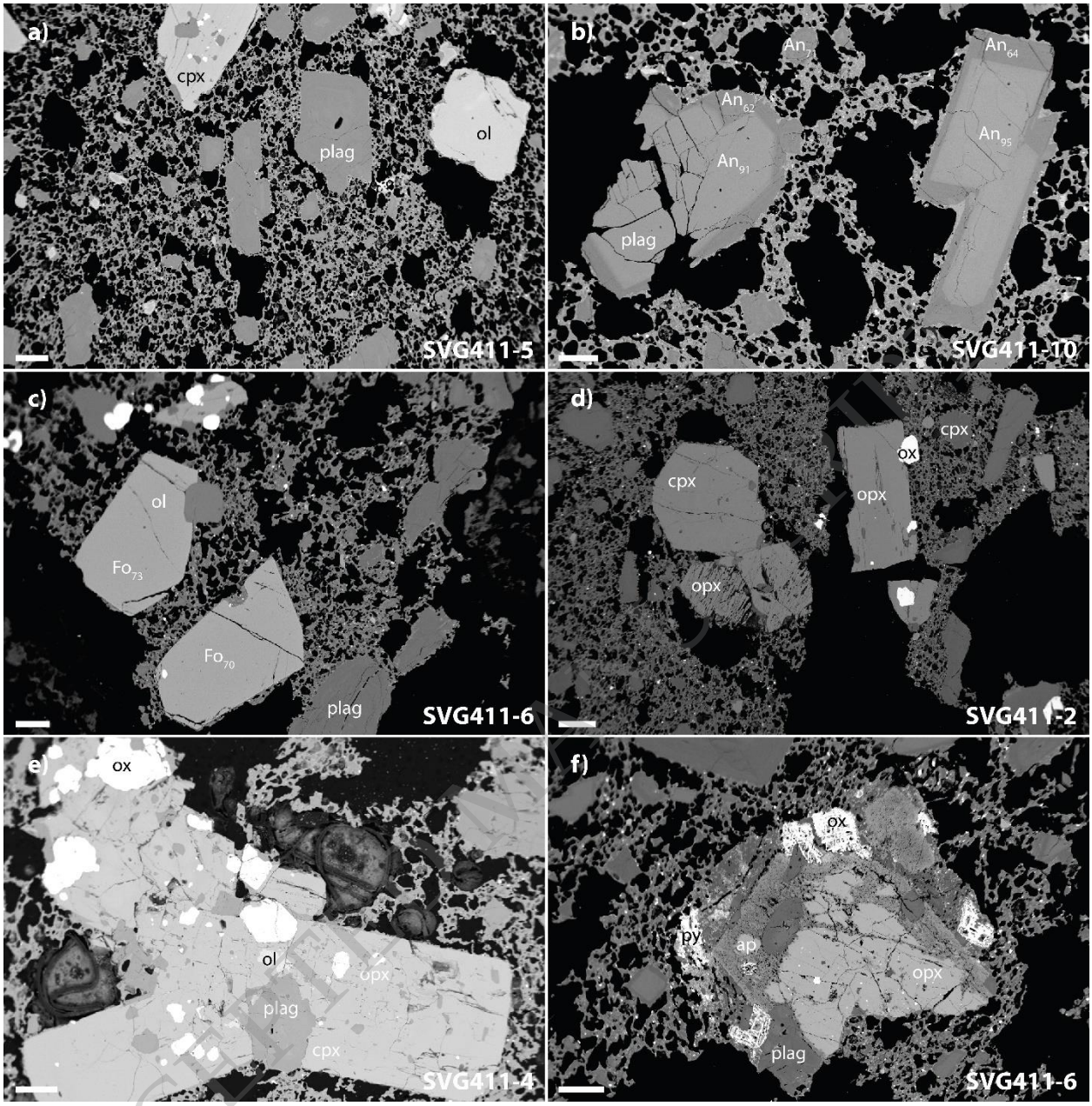

Figure 4

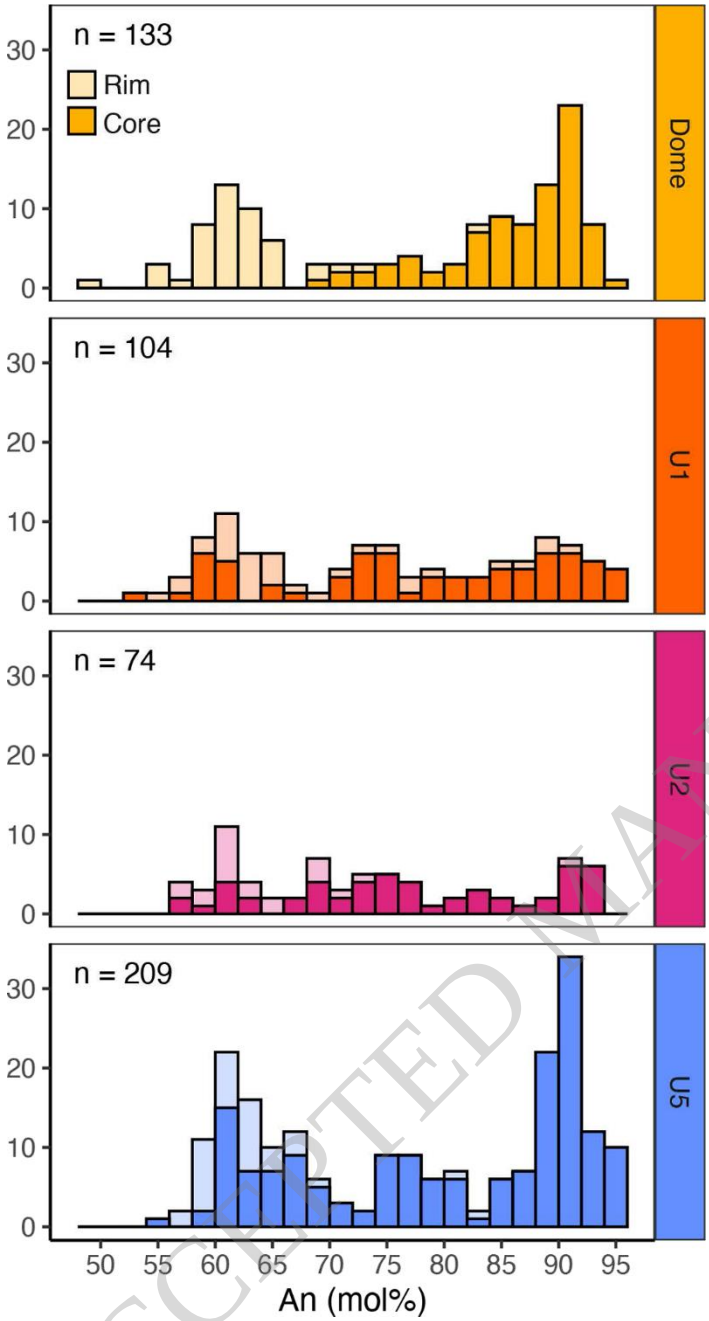

Figure 5

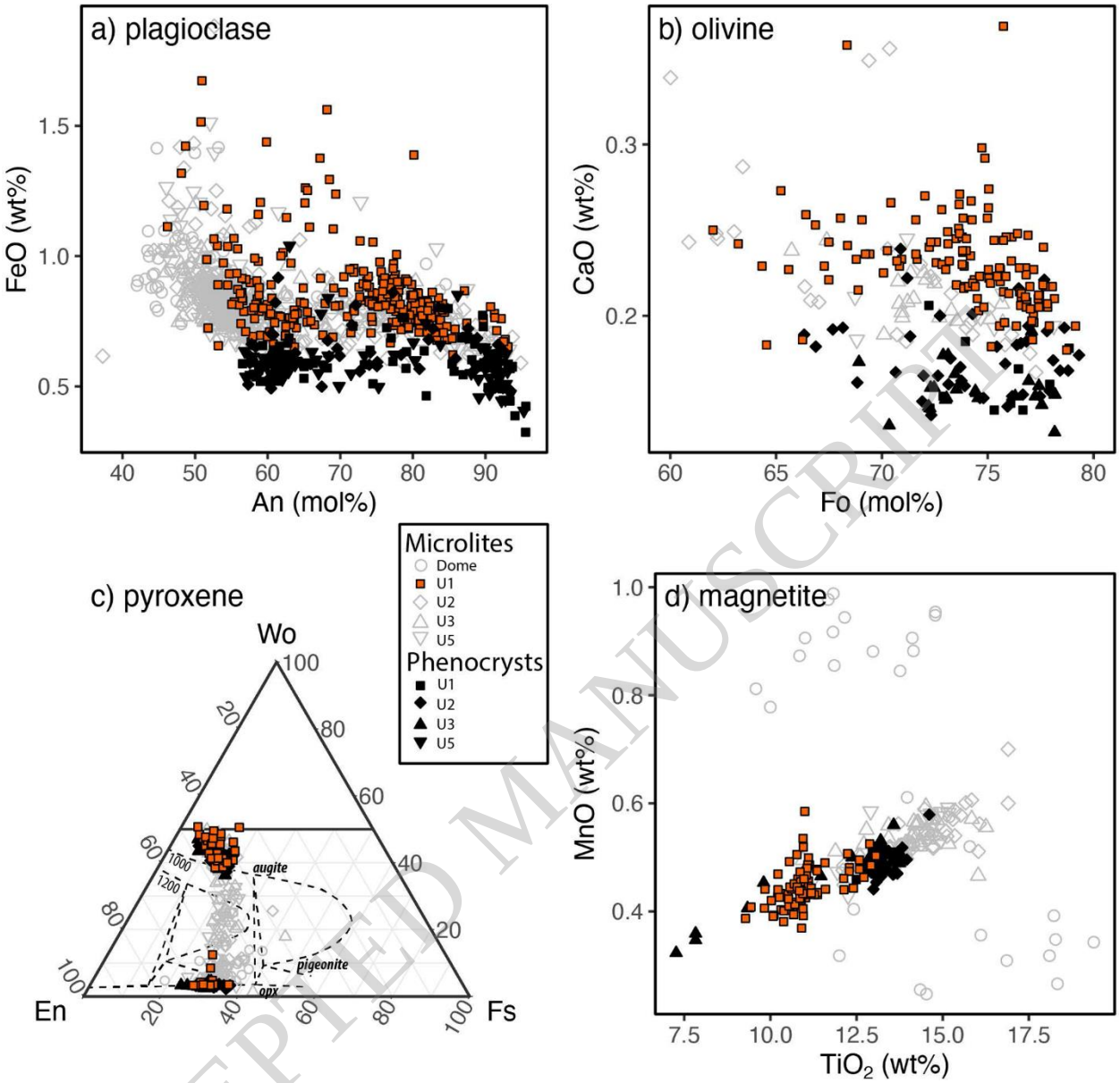

Figure 6

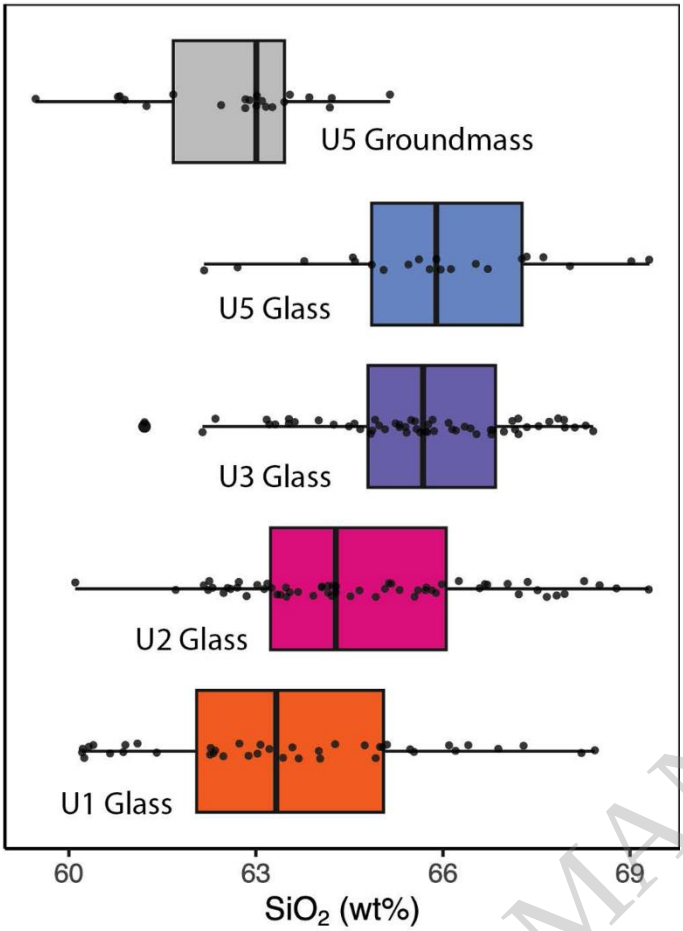

Figure 7

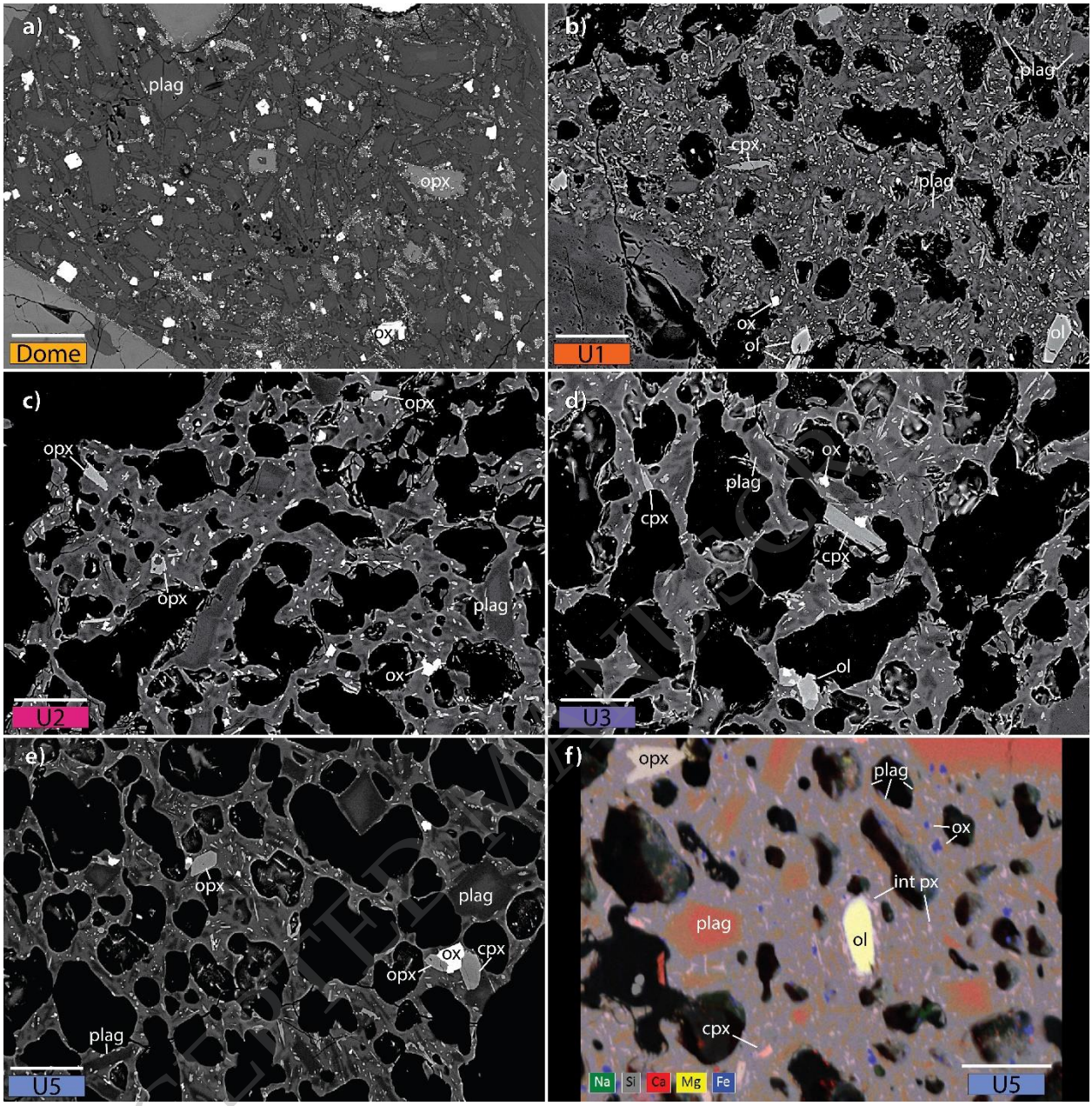

Figure 8

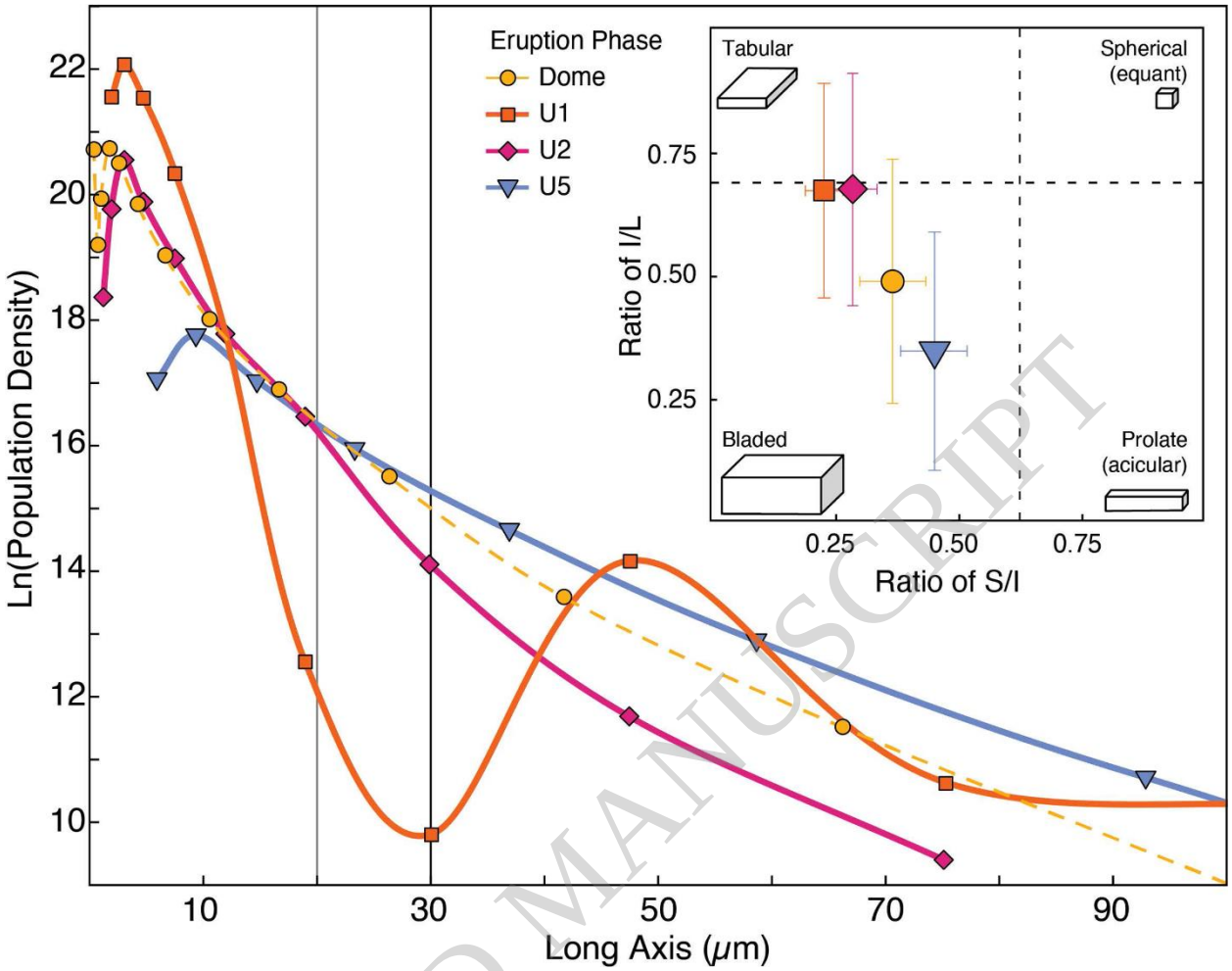

Figure 9

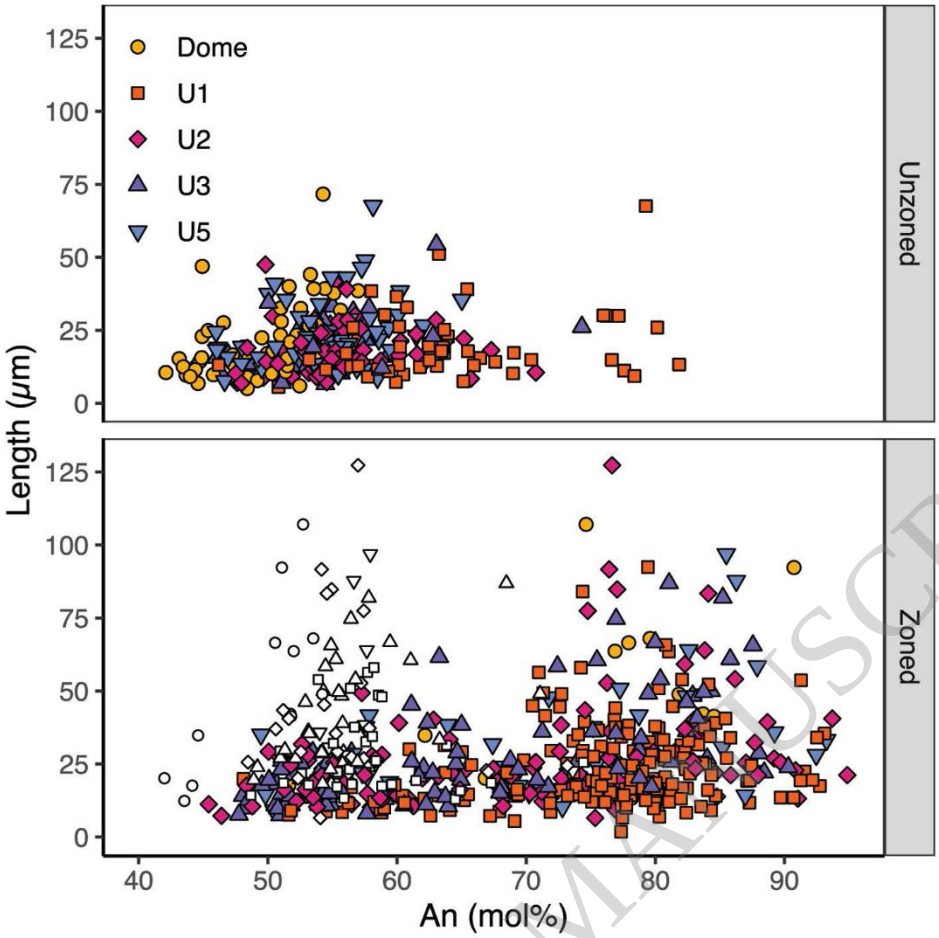

Figure 10

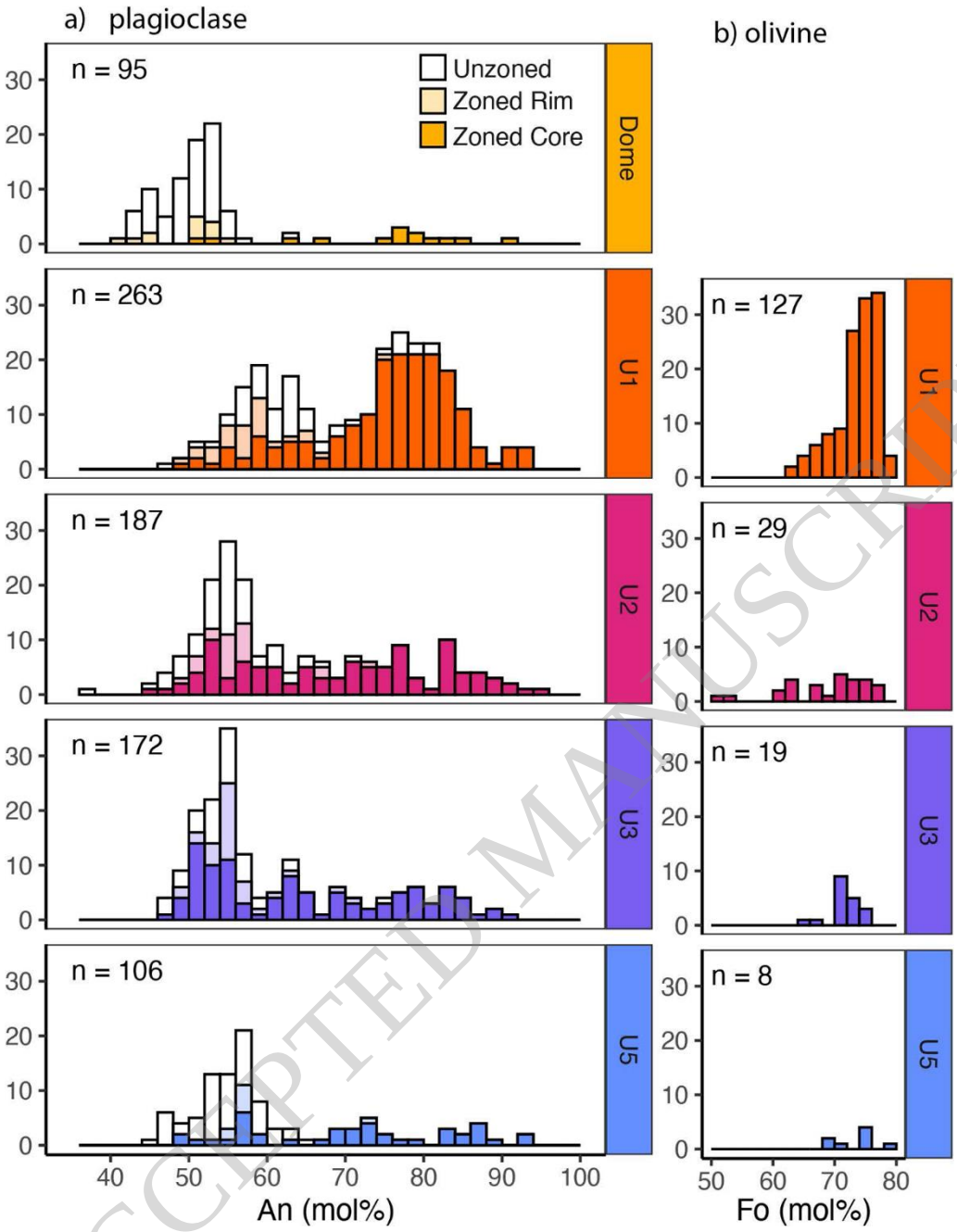

Figure 11

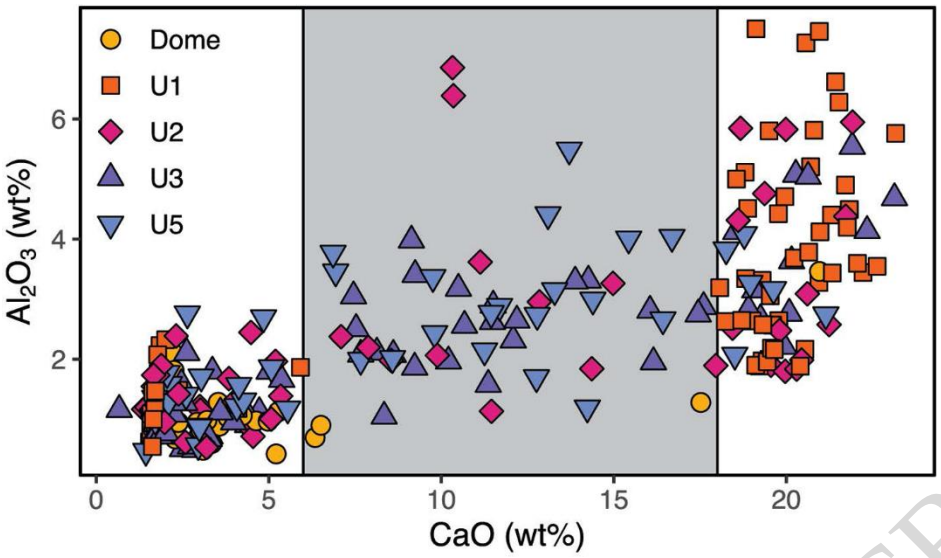

Figure 12

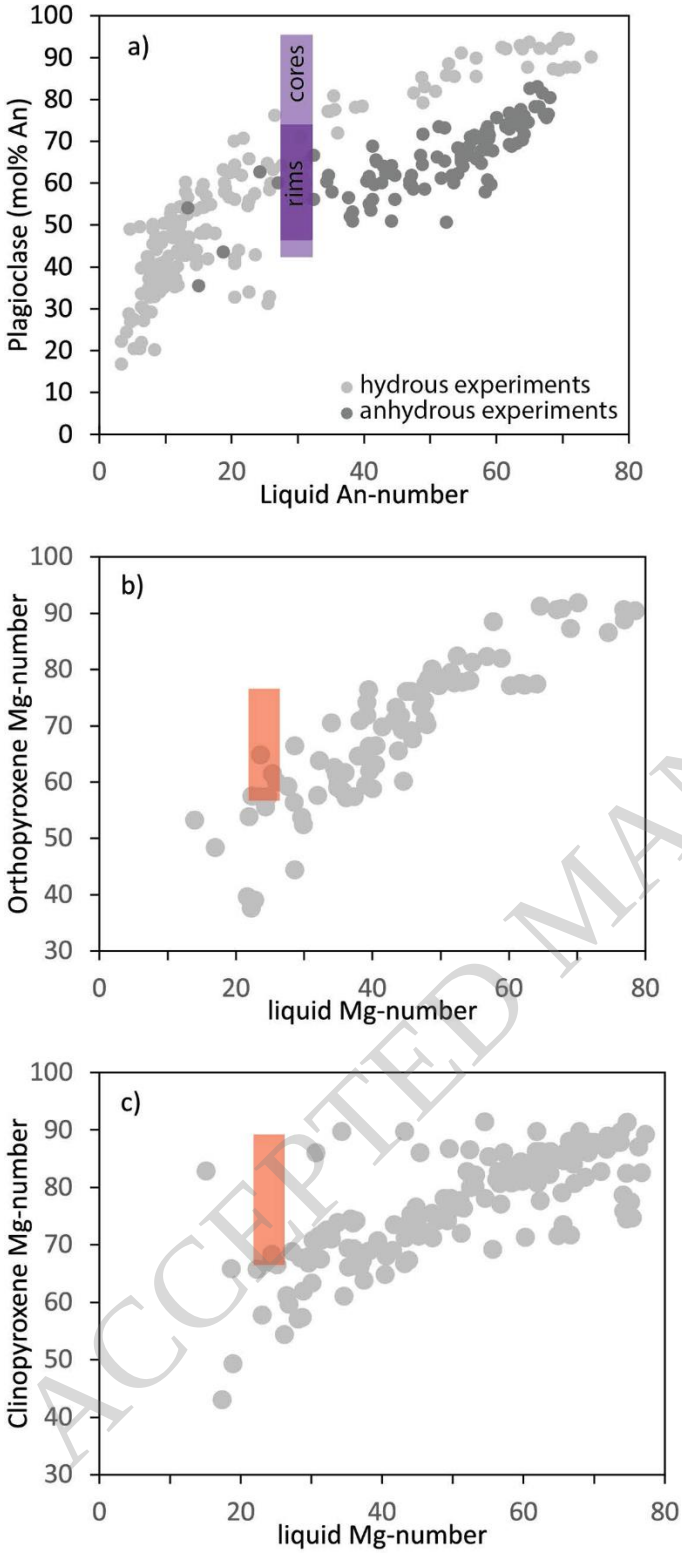

Figure 13

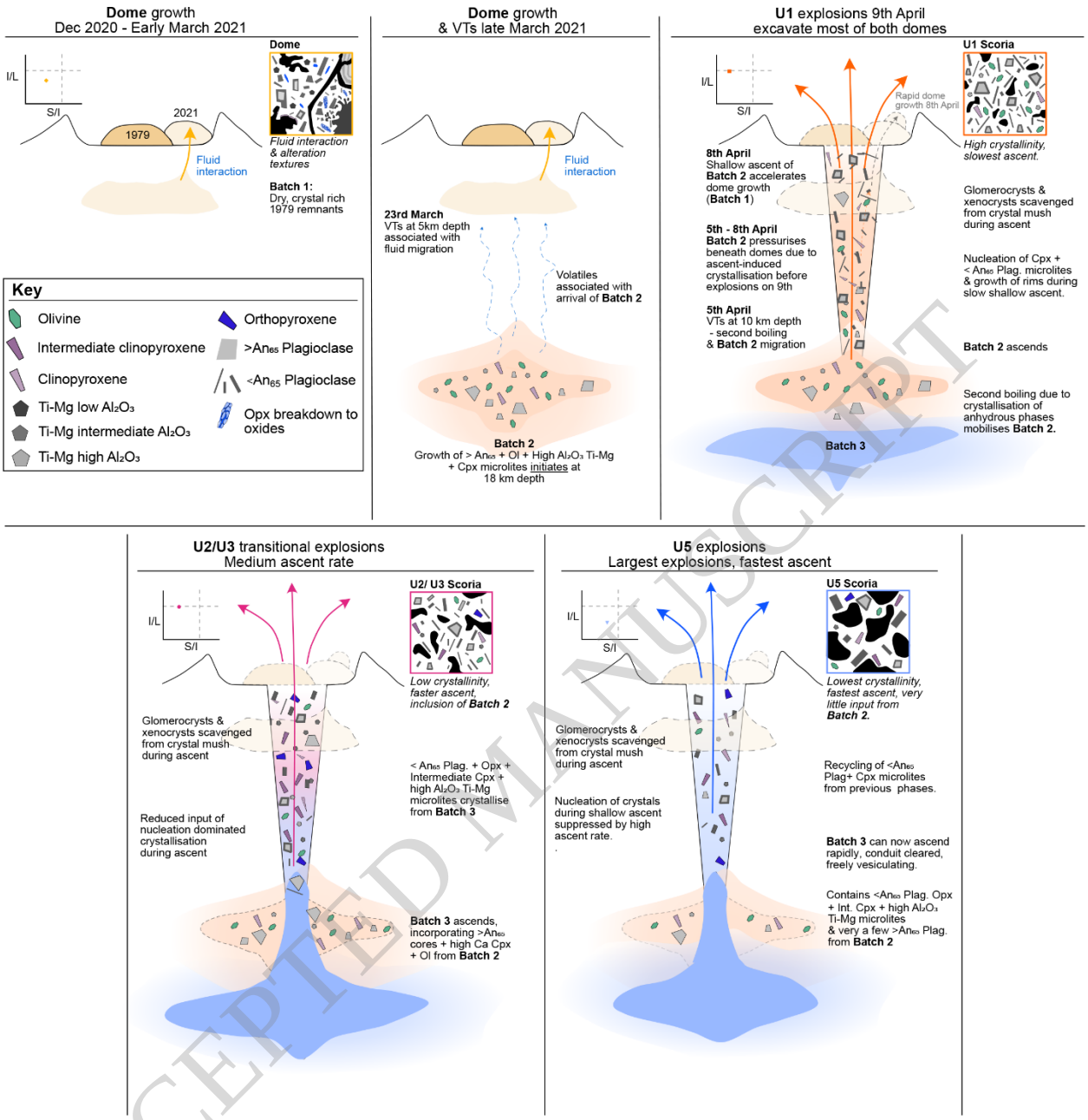

Figure 14